

1-1-2003

X-ray emission spectroscopic study of chloride solid compounds using synchrotron radiation

Ich Cong Tran
University of Nevada, Las Vegas

Follow this and additional works at: <https://digitalscholarship.unlv.edu/rtds>

Repository Citation

Tran, Ich Cong, "X-ray emission spectroscopic study of chloride solid compounds using synchrotron radiation" (2003). *UNLV Retrospective Theses & Dissertations*. 1557.
<http://dx.doi.org/10.25669/xsco-sdx9>

This Thesis is protected by copyright and/or related rights. It has been brought to you by Digital Scholarship@UNLV with permission from the rights-holder(s). You are free to use this Thesis in any way that is permitted by the copyright and related rights legislation that applies to your use. For other uses you need to obtain permission from the rights-holder(s) directly, unless additional rights are indicated by a Creative Commons license in the record and/or on the work itself.

This Thesis has been accepted for inclusion in UNLV Retrospective Theses & Dissertations by an authorized administrator of Digital Scholarship@UNLV. For more information, please contact digitalscholarship@unlv.edu.

X-RAY EMISSION SPECTROSCOPIC STUDY OF CHLORIDE SOLID
COMPOUNDS USING SYNCHROTRON RADIATION

by

Ich C. Tran

Bachelor of Science, Engineer in Physics
Hanoi University of Technology, Hanoi, Vietnam
1984

A thesis submitted in partial fulfillment
of the requirements for the

Master of Science Degree in Chemistry
Department of Chemistry
College of Science

Graduate College
University of Nevada, Las Vegas
August 2003

UMI Number: 1416257

UMI[®]

UMI Microform 1416257

Copyright 2003 by ProQuest Information and Learning Company.

All rights reserved. This microform edition is protected against
unauthorized copying under Title 17, United States Code.

ProQuest Information and Learning Company
300 North Zeeb Road
P.O. Box 1346
Ann Arbor, MI 48106-1346



Thesis Approval
The Graduate College
University of Nevada, Las Vegas

July 24, 2003

The Thesis prepared by

Ich C. Tran

Entitled

X-ray Emission Spectroscopic Study of Chloride Solid Compounds Using
Synchrotron Radiation

is approved in partial fulfillment of the requirements for the degree of

Master of Science in Chemistry

Examination Committee Chair

Dean of the Graduate College

Examination Committee Member

Examination Committee Member

Graduate College Faculty Representative

ABSTRACT

X-ray Emission Spectroscopic Study of Chloride Solid Compounds using Synchrotron Radiation

by

Ich C. Tran

Dr. Dennis Lindle, Examination Committee Chair
Professor of Chemistry
University of Nevada, Las Vegas

An x-ray emission spectrometer, developed at beamline 9.3.1 of the Advance Light Source (ALS), Lawrence Berkeley National Laboratory (LBNL), will allow performing measurements of x-ray emission from molecules and materials in gas, liquid and solid phases with energy, angle and polarization dependence. A two-dimensional position-sensitive detector system with data acquisition software is developed for the spectrometer that allows collecting a complete x-ray emission spectrum simultaneously. Mechanical supports for detector mounting and a holder for solid samples are designed and manufactured. Energy calibration, resolution, and performance of the detector system and the spectrometer are tested by studying a solid potassium chloride (KCl) sample with photon energies in the vicinity of Cl *K* edge. A detectable energy range of 55-60 eV with a resolution of 0.2 eV are obtained and reported. The detector system and data acquisition software are suitable for x-ray emission measurements.

TABLE OF CONTENTS

ABSTRACT.....	iii
LIST OF FIGURES	vi
LIST OF TABLES	vii
ACKNOWLEDGEMENTS	viii
CHAPTER 1 INTRODUCTION	1
CHAPTER 2 X-RAY EMISSION SPECTROSCOPY STUDIES WITH SYNCHROTRON RADIATION	5
2.1 Synchrotron Radiation	5
2.2 Classification of x-ray emission and related spectroscopic transitions. Selection rule.	7
2.3 Resonant XES	13
2.4 Studies with Polarized X-ray Emission Spectroscopy.....	14
CHAPTER 3 MOLECULAR ORBITAL THEORY AND CALCULATIONS.....	18
3.1 Molecular orbital theory	18
3.2 Assignment of molecular orbitals	20
3.3 Relative intensity of x-ray emission	21
3.4 Method of computation.....	22
3.5 Electronic structure of CH ₃ Cl	23
3.6 Interpretation of PXES experimental data of CH ₃ Cl	28
CHAPTER 4 DEVELOPMENT OF THE X-RAY EMISSION SPECTROMETER ..	32
4.1 XES Spectrometer.....	32
4.2 Sample holder	37
4.3 Detector system.....	38
CHAPTER 5 PERFORMANCE OF THE SPECTROMETER AND DETECTOR SYSTEM.....	48
5.1 Testing detector with a UV light source and performance	48
5.2 XAS measurement of KCl	50
5.3 Testing detector with beamline x-rays and performance of the spectrometer.....	51

APPENDIX.....	57
BIBLIOGRAPHY.....	63
VITA	68

LIST OF FIGURES

2.1	Schematic diagram of beamline 9.3.1, ALS	6
2.2	Basic x-ray absorption and decay processes. a,b). Normal x-ray fluorescence and Auger decay; c,d). Resonant absorption and decays.....	9
2.3	Efficiencies of x-ray emission (fluorescence) compared to Auger yield.....	12
2.4	Cl K-V fluorescence spectra from CH ₃ Cl following Cl $1a_1 \rightarrow 8a_1$ excitation with 2823.4 eV photon energy (Cl $1s$ absorption threshold). The labels parallel and perpendicular refer to orthogonal orientations of the measured fluorescence polarization relative to incident \vec{e} vector.[2]	16
3.1	Model of the CH ₃ Cl molecule with C_{3v} symmetry	23
3.2	XAS and NXES spectra of CH ₃ Cl. The x-ray emission spectrum was measured at photon energy of 2880 eV. On the left side is an energy level diagram of MOs involved in electronic transitions	28
3.3	Resonant XES spectra of CH ₃ Cl. The x-ray emission spectrum was measured at photon energy of 2823.4 eV. On the left side is energy level diagram of MOS involved in electronic transitions	31
4.1	Schematic diagram of x-ray emission spectrometer (XES).....	33
4.2	X-ray emission spectrometer at beamline 9.3.1, ALS	33
4.3	Schematic diagram of a variable Rowland circle spectrometer with fixed chord length for both sample-crystal and crystal-detector.....	35
4.4	Design and picture of the holder for solid samples.....	37
4.5	Schematic diagram of position sensitive detector and data acquisition system....	38
4.6	Detector head and supporting flange	39
4.7	Flow chart diagram of the data acquisition software XESDAQ for PXES	45
4.8	Flow chart diagram of “Data processing VI” block.....	46
5.1	Image of a linear testing mask recorded with a UV lamp.....	49
5.2	X-ray chlorine absorption spectrum of KCl.....	51
5.3	Image of the light spot from Si (111) wafer and elastic scattering light from KCl sample measured at 45° configuration of the spectrometer	53
5.4	Angular dependence measurement using elastic scattering x-rays from KCl sample	55

LIST OF TABLES

3.1	Optimized geometrical parameters of the CH ₃ Cl molecule.....	24
3.2	Character table of C _{3v} symmetry group	25
3.3	Shape and symmetry of molecular orbitals of CH ₃ Cl.....	26
3.4	Molecular orbital energy of the CH ₃ Cl molecule	27
3.5	Calculated population coefficients of MOs using 3-21 G basis set	27
3.6	Peak energies and assignment.....	29
5.1	Position on Y-axis of the spot lights elastically scattered from the KCl sample and diffracted from Si (111) wafer	54

ACKNOWLEDGEMENTS

The research involved in my thesis was conducted at the Advanced Light Source, Lawrence Berkeley National Laboratory. I would not have enjoyed such accomplishment if it had not been for the generosity and support of many staffs and workers at the ALS who contributed in part to the success of my research.

First, I would like to thank my graduate advisor, Professor Dennis Lindle for his dedication in developing my knowledge in the field of physical chemistry and physics of x-ray spectroscopy. Thanks for his introducing me to synchrotron radiation and letting me play in his research team, XAMS group. Thanks for his guidance and encouragement for every step of my study and research work.

I would like to thank Dr. Oliver Hemmers for the discussion in the software development and his guidance in physics of x-ray spectroscopy. Thanks to Dr. Kathleen Robins for her introducing me to theoretical calculations of molecular structure and teaching me how to do that. Dr. Wayne Stolte, Dr. Renaud Guillemin and Dr. Sung Woo Yu gave me a lot of advice and discussion in physics of x-ray spectroscopy and instrumentation development, and I thank them for that. Also, I would like to acknowledge the contributions of Dr. Wayne Stolte, Amanda Hudson and other members of XAMS group in experimental setup and instrumentation development for the research in this thesis.

I would like to thank many administrative people from the Department of Chemistry, the Graduate College and the International Student Service Office, who give me help and support for my study at the University of Nevada, Las Vegas.

Finally, I would like to thank my parents and brothers who always give support and encouragement for my study. Many thanks to my wife for her understanding, patience and support.

CHAPTER 1

INTRODUCTION

Spectroscopic measurements are powerful tools for understanding the properties of materials. Techniques such as x-ray absorption and photoemission spectroscopy are now standard tools for studying the electronic structure of atoms, molecules, and materials [1]. The application of these techniques and the interpretation of the results are especially important in the studies of exciting new materials, including strongly correlated electron systems, new superconductors, organic materials, and complex systems.

Technological advances have made possible a third generation of synchrotron radiation sources, characterized by their extremely high-brilliance in soft-x-ray and hard-x-ray regions [1]. It has been found quite powerful in studying the electronic structure of materials via x-ray emission spectroscopy (XES) using synchrotron radiation [1-4].

XES is a technique based on second-order optical processes, in which a core electron is excited by an incident x-ray photon and the resulting excited state decays by emitting an x-ray photon carrying the excess energy left by the filling of a core hole by a valence electron. Thus the information given by XES complements that given by the first-order optical processes of x-ray absorption or photoemission because it includes information on both absorption and photoemission as excitation processes and information on the intermediate excited state and its radiative decay [3]. However, the intensity of the signal

in a second-order optical process is much weaker than that in a first-order optical process because of the low efficiency of x-ray emission, especially in the soft x-ray region [5]. In order to obtain precise experimental data, we need state-of-the-art experimental instrumentation. The recent implementations of high flux, high intensity beamlines at synchrotron radiation facilities as well as highly efficient detectors are major contributors to the development of XES experiments [6].

Polarization-sensitivity studies of x-ray emission using synchrotron radiation [2,7-18] have unraveled new features that give information on geometry, orientation and symmetry of molecular structure. Theoretical methods have been developed to interpret the experimental results [2,7,16]. The polarized x-ray emission spectroscopy technique (PXES) has provided a new approach for studying properties of molecules and materials [2].

The work presented in this thesis is one part of the project of the development of an x-ray emission spectrometer at beamline 9.3.1 at the ALS, LBNL [19]. The x-ray emission spectrometer (the XES endstation) will provide a unique tool for studying the electronic structure of materials in gas, liquid and solid phases in the 2.2 to 6 keV energy range with a spectral resolution ($E/\Delta E$) of 3000-8000. By employing a curved Si (111) crystal situated on the Rowland circle in the secondary spectrometer, coupled with a double-crystal Si (111) monochromator in the primary spectrometer of the beamline, the new XES endstation will allow measurements of x-ray emission with energy, angle and polarization sensitivity.

The project of the development of the XES endstation has undergone several steps from designing to engineering and involved contribution, work of many scientists,

graduate students [19]. The design, engineering, and some of the mechanical assembly of the instrument occurred prior to my involvement with the project [20]. The current phase of the project has been assigned to the development of a two-dimensional position-sensitive detector system including the data acquisition software for the XES endstation, and to initial performance tests of the spectrometer. Those developments are the main objectives of my thesis research activities and contributions to the project that include:

1. Developed an experiment-adaptive two-dimensional position-sensitive detector system from a commercial product (Quantar Technology Inc.)
2. Designed and machined a vacuum flange and supports for holding and mounting the detector.
3. Designed and machined supports for mounting the detector and accomplished electronic devices on the spectrometer.
4. Built a dual AMD MP-2000 processor computer for digital data collecting and processing.
5. Developed a digital data collection system from a commercial digital I/O device (National Instrument Inc.), and made data cables and connectors.
6. Developed data acquisition software for the detector system using LabVIEW Graphical Programming Language (National Instrument Inc.).
7. Designed and machined a stainless steel mask to test the linearity and spatial resolution of the detector.
8. Tested the performance of the detector system and accomplished electronic devices.

9. Designed and machined a sample holder for solid samples.
10. Tested the performance of the detector system and the XES endstation with the beamline.

To realize those tasks above, it was necessary to acquire an understanding of the capabilities of the commercial products (hardware and electronic devices) and their principle of operation to find an effective and adaptive way to use these devices in accordance with the requirements of the XES experiments. Knowledge (techniques and skills) in programming in LabVIEW Graphical Programming Language was also needed for the development of the data acquisition software. Designing and engineering work was performed to machine some parts of the spectrometer (detector supports, a testing mask and a sample holder). This thesis will describe about the development of the detector system and data acquisition for the XES endstation and present the results of initial performance tests. Theoretical calculations of molecular orbitals for methyle chloride (CH_3Cl) molecules have been performed and presented to demonstrate the applicability of the PXES technique for studying the electronic structure of molecules.

This thesis is organized as follows: Chapter 2 presents a general overview on studies of XES and PXES with synchrotron radiation. Theoretical calculations of molecular orbitals are presented in Chapter 3. The instrumentation development of the XES endstation is presented in Chapter 4 with the description of the detector system and data acquisition software. The performance testing of the detector system, the data acquisition software, and the spectrometer is presented in Chapter 5. Designs of machined parts for the spectrometer as well as the source code of the data acquisition software are given in the Appendix of the thesis.

CHAPTER 2

X-RAY EMISSION SPECTROSCOPY STUDIES WITH SYNCHROTRON RADIATION

The electronic structure of atoms and molecules has long been studied through the interpretation of x-ray absorption and x-ray emission spectra. X-ray emission spectroscopy (XES) has a proven history of unraveling core-level phenomena in atoms, molecules and solids [3]. Traditionally, XES relied upon incident excitation by x-rays, either from conventional anode tubes with fixed-wavelengths or polychromatic sources (white light), or by high-energy electron impact. However, the limitation in selectivity of excitation-energies or the lack of sufficient x-ray intensity of the traditional excitation sources was the main obstruction in the development of XES techniques. Synchrotron-radiation sources in the x-ray energy range have shown great potential for XES, in particular, providing sufficiently intense tunable (and polarized) x-rays throughout the near-threshold regions of the core levels of most elements [1].

2.1. Synchrotron radiation

Synchrotron radiation has certain characteristics [1,5], such as high brightness, tunability (or selectivity), a pulsed nature (time resolution), and linear polarization. These

properties of synchrotron radiation, individually or combined, allow performing experiments not otherwise possible.

In the present study, x-rays from the Advanced Light Source (ALS) and energy selected by beamline 9.3.1 are used. Beamline 9.3.1 is a bend-magnet beamline that provides high-resolution x-ray beams for electron, ion, and x-ray spectroscopy measurements in atomic, molecular, and materials science [21]. The beamline is built around a double-crystal monochromator providing higher-energy x-rays than are available at most other beamlines at the ALS. By accepting up to 8 horizontal *mr*ad from an ALS bend magnet, the beamline delivers $>10^{11}$ photons/s over most of its photon energy range (2.2 to 6 keV) with a spectral resolution ($E/\Delta E$) of 3000-8000. An estimation of $\geq 99.9\%$ (at Cl *K* edge) linear polarized monochromatic x-ray beam is focused onto the sample. Figure 2.1 shows a schematic diagram of the beamline.

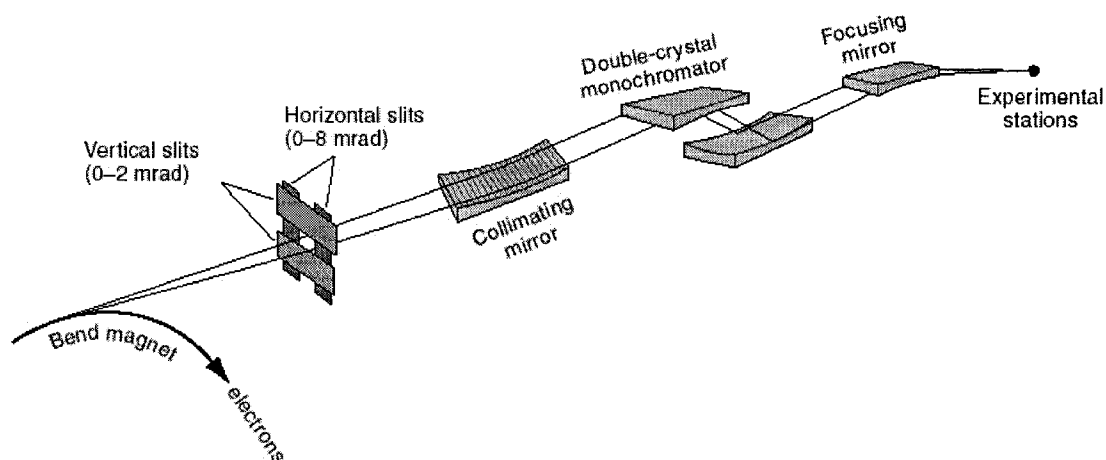
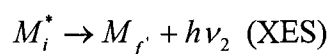
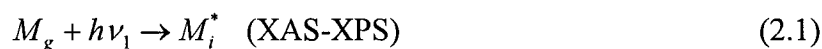


Figure 2.1: Schematic diagram of beamline 9.3.1, ALS

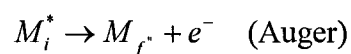
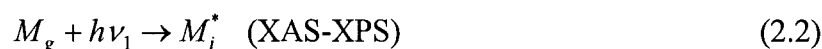
2.2. Classification of x-ray emission and related spectroscopic transitions. Selection rule

X-ray emission is a second-order optical process which occurs by the radiative decay of the final states of the first-order optical processes, X-ray absorption or X-ray photoemission. Therefore, XES is described theoretically by a coherent second-order optical formula [22].

In the x-ray absorption process the target-molecule M is excited from the ground state $|g\rangle$ to an excited state $|i\rangle$ by absorption of the incoming x-ray photon with frequency ω_1 , wave vector k_1 and polarization vector e_1 . The excited state is metastable and can therefore decay to the final state $|f\rangle$ emitting x-ray photons with frequency ω_2 , wave vector k_2 and a polarization vector e_2 :

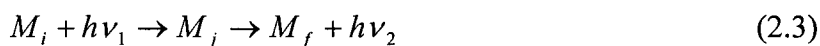


or emitting an Auger electron:



If the core electron is excited to the high-energy continuum well above the absorption threshold (as in the process of x-ray photoemission spectroscopy, XPS), the x-ray emission spectral profile is practically independent of the excitation energy. Because of this fact a two-step model with the emission decoupled from the excitation applies as shown in Eq. 2.1. This type of XES (Fig. 2.2.a) is denoted as *normal x-ray emission spectroscopy* (NXES).

On the other hand, if the core electron of the molecule M is *resonantly* excited from the initial ground state M_g near an absorption threshold by the incident photon (XAS), the resulting emission spectrum depends strongly on the incident-photon energy $E_1 = h\nu_1$ [23-26]. This type of XES (Fig. 2.2.c) is denoted as *resonant x-ray emission spectroscopy* (RXES). The shapes of resonant x-ray emission spectra are dependent on the manner of preparation of the core excited state of the target, and a one-step model with the excitation and the deexcitation treated as one, non-separable, scattering event must then be used [24]



The final states of XAS and XPS are the same as the intermediate states of RXES and NXES, respectively.

In a resonant excitation the core electron is promoted to an unoccupied bound orbital. The fluorescence decay may then occur either via a *spectator transition*, where an electron from one of the occupied orbitals fills the core hole while the excited electron remains as a spectator in the (previously) unoccupied orbital, or via a *participator transition*, where the excited electron itself fills the core hole [27]. In the participator transition, the emitted-photon energy $E_2 = h\nu_2$ is the same as that of the incident-photon energy $E_1 = h\nu_1$ and the process is called “*Rayleigh scattering*” or “*resonant elastic scattering*”, while in the spectator transition, $E_2 \neq E_1$, and the process is called “*resonant inelastic x-ray scattering*”. The final state of a spectator transition is a valence-excited state whereas the final state of a participator transition is the electronic ground state. The spectator emission peaks will be designated by the symmetry of the occupied valence orbital from which the electron filling the core hole comes.

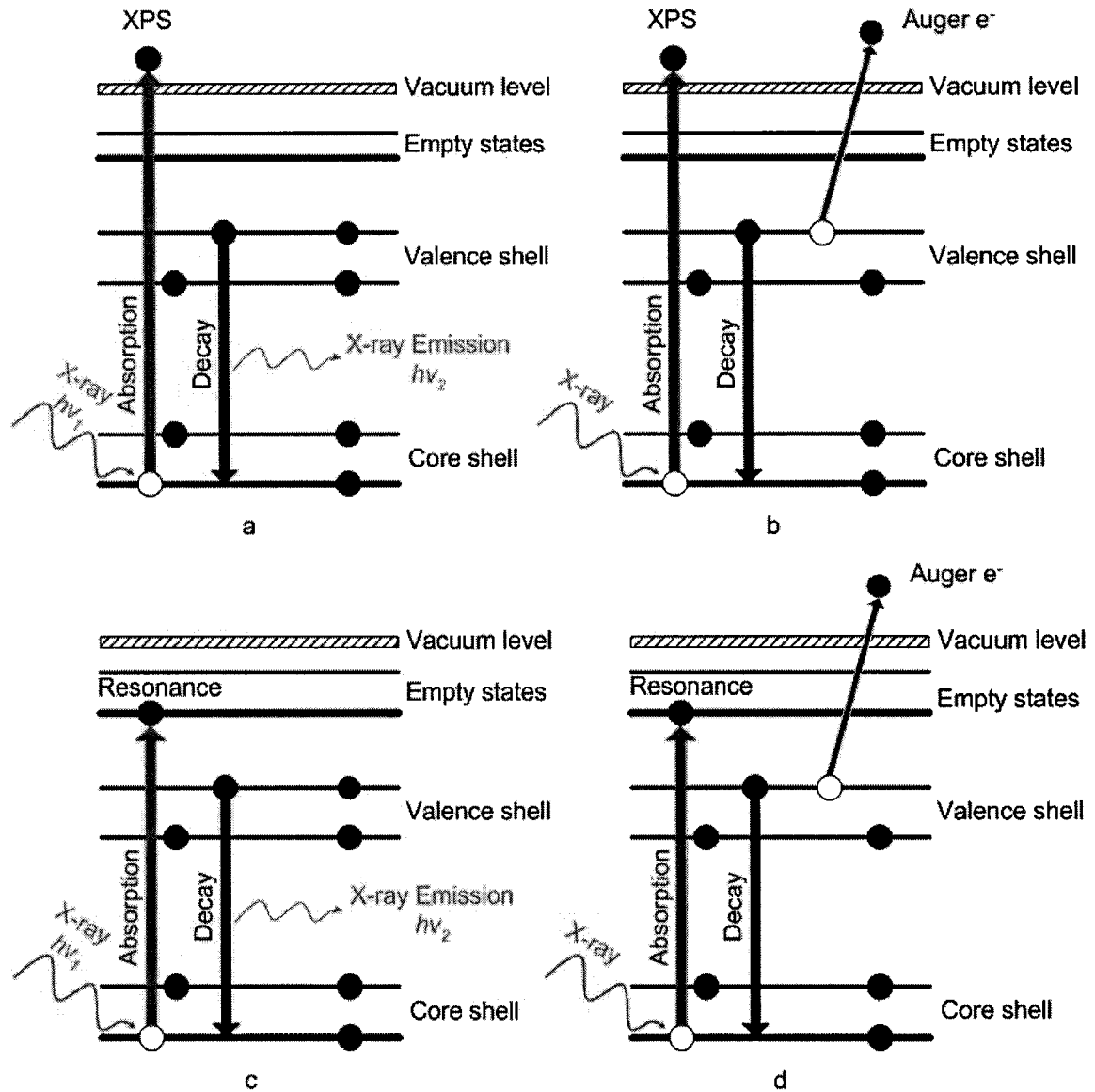


Figure 2.2: Basic x-ray absorption and decay processes. a,b). Normal x-ray fluorescence and Auger decay; c,d). Resonant absorption and decays

Within the *single-particle approximation* [27], it has been shown that the x-ray absorption and emission processes can be described as a dipole transition of photons between two electronic states. In case of x-ray emission, one has a core excited initial state and a valence excited final state. The intensity of this particular transition is given by Fermi's Golden rule:

$$I_{XES}(E) \propto E_{if}^3 \left| \langle \Psi_f | \hat{V} | \Psi_i \rangle \right|^2 \delta(E_{if} - E) , \quad (2.4)$$

where Ψ_i and Ψ_f are the total wave functions of the initial core vacancy state (recall that it is the intermediate state in a one-step model of XES), and final valence excited state. E_{if} is the energy difference between the two states $E_{if} = E_i - E_f$. \hat{V} is an operator describing the interaction between photons and electrons. Since the wavelength of the x-ray is longer than the atomic dimensions, one can make a simplification by an approximation with good validity, *the dipole approximation*:

$$\hat{V} \propto \vec{r} \cdot \vec{e} = \hat{D} \quad (2.5)$$

where \vec{r} is transition matrix element and \vec{e} is the polarization vector of the emitted radiation.

The dipole approximation leads to certain selection rules that limit the states *allowed* to participate in a dipole transition. The angular momentum has to change by one: $\Delta l = \pm 1$, the z-component, m , of the orbital momentum has to change by $\Delta m = \pm 1, 0$ and the spin has to be conserved: $\Delta s = 0$. This implies that if a *1s*-core electron is excited one observes the unoccupied levels of *p*-character. Similarly the excitation of a *p*-core electron probes the unoccupied levels of *s*- and *d*-character. The ionization threshold (ionization potential - IP) is reached if the x-ray energy $h\nu_1$ is exactly equal to the binding energy of the core hole (E_{1s}). The unoccupied levels are then reproduced by the XAS spectrum with energies $E_{unocc} = E_{1s} + h\nu_1$, with the *1s* binding energy given as a negative number.

The same core hole excitation process can excite an electron out of a molecule. Its kinetic energy (E_k) can be detected and gives directly the binding energy (E_c) of the core electron as: $E_c = E_k - h\nu_1$, with the binding energy given as a negative number.

The core hole decay can take place radiatively by a x-ray emission (XES) process or non-radiatively by an Auger process (AES). XES follows the same selection rules as x-ray absorption and a $1s$ -core hole can be filled by a core $2p$ -electron or a valence p -electron. If a $2p$ -core electron fills the $1s$ -core hole the x-ray energy gives the difference in binding energy of the two core states $E_{2p} - E_{1s} = h\nu_2$ and the final state contains one $2p$ -core hole (M_f in Eq. 2.1). If a valence p -electron fills the $1s$ -core hole the XES spectrum maps out the occupied valence orbitals: $E_{occ} = h\nu_2 + E_{1s}$.

The primary example of non-radiative decay is the Auger process, in which one $2p$ -electron fills the $1s$ -core hole and the excess energy is transferred to another $2p$ -electron so that it is excited out of the molecule as a free electron. In this $1s$ - $2p2p$ Auger process the final state contains two $2p$ -core holes (M_f in Eq. 2.2). The kinetic energy of the emitted electron approximately equals $E_k = E_{2p} + E_{2p} - E_{1s}$. If a $2p$ -core electron and a valence electron take part in the Auger process one can detect again the occupied valence state $E_{occ} = E_k - E_{2p} + E_{1s}$. It is also possible that two valence electrons take part in the Auger process (Fig. 2.2.b and 2.2.d). The Auger decay can also occur via a *spectator transition* or via a *participator transition* as the x-ray emission decay.

X-ray emission and Auger decay are, in fact, competitive processes, and the x-ray emission efficiency is quite low in the soft x-ray region compared to the Auger efficiency. Figure 2.3 shows the fluorescence and Auger yields for $1s(K)$ and $2p_{3/2}(L_3)$ subshells of

different atoms [5]. For light atoms, the fluorescence efficiency is less than a few percent and the Auger yield is larger than the fluorescence yield. The Auger yield decreases while the fluorescence yield increases as the atomic number Z increases. There is a crossing around Zn for K shell.

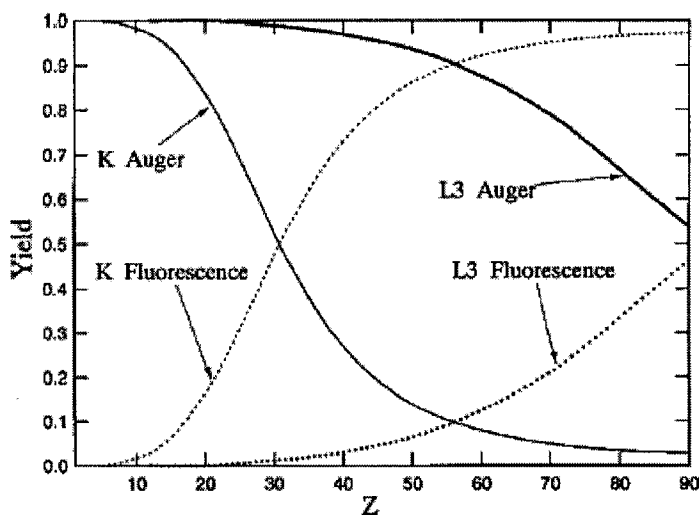


Figure 2.3: Efficiencies of x-ray emission (fluorescence) compared to Auger yield.

One direct consequence of dipole selection rules on molecules with high symmetry is related to the parity. In a molecule with inversion symmetry, like Cl_2 , there are states with two different parities, even (g - *gerade*) or odd (u - *ungerade*) transforming as +1 or -1 under the inversion operator. Since the dipole operator (\vec{r}) is odd, the matrix element in Eq. 2.4 vanishes if the two wave functions are of the same parity. Thus, the dipole selection rule requires that only transitions involving $g \rightarrow u$ or $u \rightarrow g$ are *allowed*, while the transitions with the same parity are *forbidden*. However, experimental measurement of high-resolution x-ray emission in Cl_2 [7] has shown evidence of nondipole transitions.

2.3. Resonant XES

So far, core hole creation (XAS) has been described separately from core hole decay (XES and AES). However as soon as core hole creation takes place decay occurs. This implies that close to the x-ray absorption resonances, the decay processes can be different from off-resonance excitations. Indeed, capability of selective excitation with synchrotron radiation provides opportunities for many studies of resonant x-ray emission spectroscopy that revealed a wealth of information on resonant and multivacancy effects in x-ray spectra not previously attained in off-resonant or normal XES [8,28]. By selectively tuning the incident radiation to the near-threshold excitation of core states, less complex x-ray emission spectra are obtained, and therefore more characteristic features of electronic transitions can be identified [28]. This reduction in complexity is attributed to the enhancement of transitions at resonance and the elimination of multielectron transitions, which commonly produce satellite features in x-ray emission [26].

The traditional two-step formulation [29,30], which assumes the x-ray emission to be decoupled from the x-ray absorption process, has applicability in the nonresonant case far from threshold, but only in special cases for near-threshold excitation. The popularity of that model stems from its simplicity and from its applicability to nonresonant x-ray emission [29]. However, application of the quantum-theoretical version of the two-step model to molecules is complicated by the need to account for rotational transitions in absorption and emission and for resonant emission it is necessary for each given case to inspect the applicability of this model. A more accurate picture may be that of a one-step, inelastic scattering process by molecules essentially fixed in space during the time scale

of the process [2]. Interpretation of nonresonant x-ray emission as a one-step process was proposed in the 1970s by Gel'mukhanov and co-workers [24,31-33] who introduced the notion of x-ray channel interference, and applied this to investigations of x-ray scattering in solids and molecules, and to vibronic fine-structure analysis of x-ray spectra. Several different features of resonant x-ray emission spectra, such as lifetime vibrational and electronic state interference effects, screening effects, vibronic coupling and symmetry breaking, and angular dependence, have been obtained from this model [34-38] for molecules in gas phase and solid materials. A review on recent studies of resonant x-ray emission spectroscopy in solids is given in [39].

2.4. Studies with Polarized X-ray Emission Spectroscopy

The technique of polarized x-ray emission spectroscopy (PXES), which is the main focus of this thesis, combines the advantages of monochromatic synchrotron radiation (tunability, polarized excitation) with polarization analysis of the x-ray fluorescence. In x-ray absorption spectroscopy, alignment and bonding geometry have been studied by using the defined polarization of synchrotron radiation. In x-ray emission this is certainly also an available technique that offers many interesting opportunities [1]. Applications of the PXES technique to study electronic structure of molecules and materials have unraveled anisotropic features of x-ray emission that give geometrical and symmetry information on molecular structure [2].

It is generally assumed that x-ray emission is isotropic and the observation of anisotropic x-ray emission from molecular crystals and solids has been attributed to the inherent ordering of those samples. It has been expected that randomly oriented samples,

such as gas-phase molecules, will display isotropic x-ray emission. However, resonant excitation by a photon or particle beam will generally leave an atomic or molecular target in an anisotropic state, and this anisotropy is manifested in the polarization and angular distribution of emitted photons [29,30,40]. The dipole nature of the x-ray absorption and linear polarization of the excitation radiation create an uneven distribution of excited molecules with respect to their orientation in space by selectively populating a subset of the randomly oriented molecules. One, therefore, can expect to observe the anisotropy of x-ray emission from molecule excited by linearly polarized synchrotron radiation. The first observation of strongly anisotropic polarized x-ray emission from gas-phase molecules following energy-selected and polarized excitation near-threshold [28] was reported by Lindle and co-workers [2]. Polarized excitation to states of particular molecular symmetry produces aligned intermediate states, and therefore results in strongly polarized and anisotropic x-ray emission. The polarization selectivity of the emission spectrometer was used to distinguish emission polarized parallel or perpendicular with respect to the polarization of the exciting radiation (Figure 2.4). It has been shown that the polarized x-ray emission technique can be used to infer, directly from experiment, symmetries of occupied and unoccupied valence molecular orbitals, anisotropies in absorption and emission, and orientational and geometrical information.

In the hard x-ray region (>1000 eV), a number of studies on polarization effects of x-ray emission have been reported. Studies on the polarization dependences of Cl $K-V$ x-ray emission from Cl-containing molecules (methyl chloride, CH_3Cl , and the chlorofluoromethanes, CF_3Cl , CF_2Cl_2 , and CFCl_3) [2,8-10], and S $K-V$ x-ray emission from H_2S [11] and COS [12] have been performed using the technique of polarized x-ray

emission spectroscopy. The degree and the orientation of the polarized emission are observed to be sensitive to the incident excitation energy near threshold. Distinctively different angular distributions are observed for x-ray emission involving molecular orbitals of different symmetries.

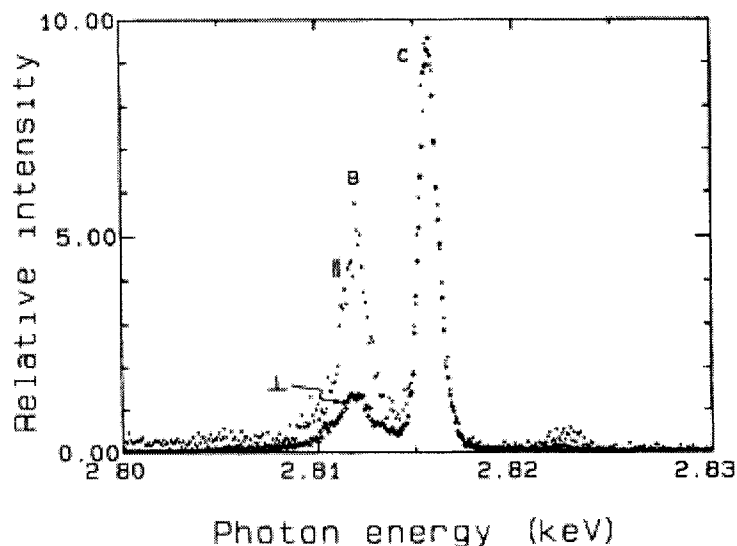


Figure 2.4: Cl K-V fluorescence spectra from CH_3Cl following Cl $1a_1 \rightarrow 8a_1$ excitation with 2823.4 eV photon energy (Cl $1s$ absorption threshold). The labels parallel and perpendicular refer to orthogonal orientations of the measured fluorescence polarization relative to incident \vec{e} vector.[2]

In the soft x-ray region (<1000 eV), the technique of polarized x-ray emission spectroscopy has also been applied to investigate the electronic structure of CO_2 [13], O_2 [14], and graphite [15]. The angular dependence of resonantly excited x-ray emission spectra has been interpreted by treatment with a one-step formalism for the resonant inelastic x-ray scattering process [16] and used to assign symmetries of the states involved [17].

Thus, the core-level polarized x-ray spectroscopy technique has provided a new approach to molecular photoabsorption and emission, and has been proven a powerful tool in molecular-structure studies [1,18]. The following chapters are devoted to theoretical studies and development of instrumentation for application of this technique to the study of molecules and materials.

CHAPTER 3

MOLECULAR ORBITAL THEORY AND CALCULATIONS

XES and XAS can be used to study electronic structure of occupied and unoccupied molecular orbitals (MOs) [22,27]. Polarization effects of XES provide details on the symmetry of MOs and help in assigning MOs to the spectrum [2,17]. Theoretical electronic structure calculations of molecules can predict possible electronic transitions and help in the interpretation of experimental results by identifying features of the spectrum. Comparisons between experimental spectroscopic data and theoretical calculations are essential in understanding electronic structure of molecules. In this chapter, theoretical calculations for MOs of methyle chloride (CH_3Cl) molecule are presented for interpretation of experimental data from literature [2,10] and for demonstration of the PXES technique.

3.1. Molecular orbital theory

In molecular quantum mechanics, two approximate methods most commonly used to describe electronic structure of molecules are the valence bond theory and molecular orbital theory [27]. While valence bond theory emphasizes the bond as a distinct atom-atom entity in the molecule, and concentrates on pairs of electrons, the molecular orbital method views molecules as a continuous electron distribution and less as a collection of

identifiable bonds. This is, therefore, an advantage in using molecular orbital theory to describe electronic structure of molecules when the spectroscopic properties are being considered [22,27]. In this method, the MOs are often approximated by a linear combination of atomic wave functions (atomic orbitals, AOs), which are localized on individual atoms in the molecule.

$$LCAO - MO = \sum_n C_n \Psi_{AO}^n \quad (3.1)$$

where, Ψ_{AO}^n is the atomic wave function of the n-th electron in the molecule.

Calculation using molecular orbital theory describes simple molecules accurately and provides sufficiently good approximations of the electronic structure for many complex molecules. With the recent development of supercomputers and algorithms, computation time required for these calculations is reasonable and many computer programs are available. Theoretical background for the computational treatments and modeling of electronic structure is given in common quantum chemistry and physical chemistry textbooks [41,42]. One of the most popular packages of programs for electronic structure calculation is Gaussian [43] (now version 2003). One also can run calculations with Gaussian software by accessing a server version (WebMO) [44]. Alternative software is Hyperchem (release 7.0) from HyperCube Inc.[45] that also allows performing different methods of calculation on the electronic structure of molecules, such as *ab initio*, semi-empirical and density functional theory as with Gaussian software package. The internal rendering unit of Hyperchem software can also give the picture of calculated MOs. One useful feature of Hyperchem is its “Crystal” unit, which performs simple calculations for electronic structure of solid crystals. For advanced treatments, however, method employing “Band Theory” [46] needs to be used to obtain a more accurate picture of

electronic structure of solid and periodic systems, for example, the linear muffin-tin orbital (LMTO) method [47].

3.2. Assignment of molecular orbitals

The electronic configurations of molecules can be established using the molecular version of the build-up principle [27,41]. We decide what orbitals are available, judge the order of their energies and then feed in the appropriate number of electrons into the lowest available orbitals consistent with the Pauli Exclusion Principle. Assignment of MOs from AOs for diatomics is straightforward. In order for orbitals to overlap and participate in bonding, they must have similar energies and the same symmetry with respect to rotation about the internuclear axis. For polyatomic molecules, the assignment procedure is more complicated. However, the idea introduced for diatomic molecules, and in particular the role of the overlap of AOs, is the basis for the assignment of MOs. Concepts of group theory for molecular symmetry can be useful in this procedure.

The symmetry of the overlap is used to distinguish between the various types of MOs. For a linear molecule, if the overlap is symmetrical for rotation about the molecular axis, then the MO obtained is a σ -orbital. If the overlap has a nodal plane along the molecular axis, the resulting MO is a π -orbital. The MO obtained from an overlap which has two nodal planes intersected along the molecular axis is a δ -orbital. The overlap between the three p AOs, p_x , p_y , and p_z , in two atoms results in one σ -type MO for the overlap between two p_z orbitals, and two π -type MOs for the overlaps between two corresponding p_x and p_y orbitals, denoted as π_x and π_y , respectively. These MOs, π_x and π_y , have the same energy and are equivalent in the molecule. But the overlap integral of the π -bond is

smaller than overlap integral of σ -bond, therefore π -bonding will have energy smaller than σ -bonding. The σ -anti-bonding has higher energy than π -anti-bonding.

3.3. Relative intensity of x-ray emission

Another direct consequence of dipole selection rules for x-ray emission spectroscopic transitions (Chapter 2) is that one can estimate the relative intensity of XES spectrum [42]. When modeling the electronic structure of molecules with wave functions as a linear combination of atomic orbitals (LCAO-MO), the spectral intensity of XES can be approximated by simpler methods than calculating the full wave functions of the two states in Eq. 2.4, using the fact that the core hole states are localized in space to particular atoms of the molecule [27]. Exemplifying this with K emission, the core excited state can be expressed as only a $1s$ wave function $\chi(1s)$. The intensity of the x-ray transition, Eq.1.4 can be written as:

$$I_{XES}(E) \propto E^3 \left| \langle \Psi_f | \hat{D} | \chi(1s) \rangle \right|^2 \quad (3.2)$$

Since Ψ_f can be represented by a linear combination of atomic orbitals (Eq. 3.1):

$$\Psi_f = \sum_n C_n \chi_n \quad (3.3)$$

which gives the intensity as:

$$I_{XES}(E) \propto E^3 \left| \sum_n C_n \langle \chi_n | \hat{D} | \chi(1s) \rangle \right|^2 \quad (3.4)$$

If we further take into account only the one-center term (with the assumption that core excited states are localized on atoms in a molecule) , i.e. the contribution from the

allowed orbital χ_p centered on the same atom as the core state, and neglect the slowly varying E^3 term, the intensity is given simply by:

$$I_{XES}(E) \propto \left| \langle \chi_p | \hat{D} | \chi(1s) \rangle \right|^2 \propto C_p^2 \quad (3.5)$$

Thus, the relative intensity of x-ray emission is proportional to the population of atomic- p -character molecular orbitals on specific atoms of the molecule.

In solid samples, discrete states of atoms or molecules are transformed to continuous bands. How will the x-ray intensity best be described in that situation?. In principle, the same argument as described above that leads to the one-center approximation in molecules can be used to calculate the intensity. Instead of using the population coefficient C_p , the intensity is governed by the density of states (DOS). Thus, in a K spectrum, where a $1s$ core hole is created, only states with p character are allowed to decay and a partial p -type density of states DOS_p is measured within the localized and one-particle model for a solid material. The intensity is given by:

$$I_{XES}(E) \propto E^3 DOS_p(E) \quad (3.6)$$

Since the measured XES spectrum maps out the partial DOS , it can be used to study the electronic structure of solid materials, for example to find the band gap, the highest or lowest edges of the valence band, in a complementary way to other spectroscopic techniques.

3.4. Method of computation

All calculations on the MO energies of CH_3Cl have been performed by *ab initio* method on the Hartree-Fock (H-F) levels using the Gaussian software [44] with the 3-

21G, 6-31G(d) and 6-31G(d,p) basis sets. First, geometry is optimized with the Berny algorithm using 6-311G(d,p) basis set. An excerpt from the Gaussian output data file for the optimized geometrical parameters of the CH_3Cl molecule is presented in Table 3.1. The optimized Z-matrix is used as input Z-matrix for other molecular orbital energy calculations. The final MOs are rendered and viewed by MOView software [44]. Calculations have also been performed using Hyperchem software, which gives the similar results as with the Gaussian software when using the same basis set and procedure.

3.5. Electronic structure of CH_3Cl

The methyl chloride (CH_3Cl) molecule belongs to the C_{3v} symmetry point group with a C_3 rotational axis along the molecular axis Z (C-Cl axis), and 3 vertical mirror planes σ_v , which contain the Z-axis and bisect the angles H-C-H, as shown in Fig. 3.1.

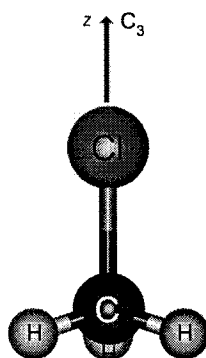


Figure 3.1: Model of the CH_3Cl molecule with C_{3v} symmetry

Table 3.1: Optimized geometrical parameters of the CH₃Cl molecule

```

CH3Cl-6311G(dp)
-----
Symbolic Z-matrix:
Charge =  0 Multiplicity = 1
C
Cl          1      B1
H           1      B2          2      A1
H           1      B3          2      A2          3      D1          0
H           1      B4          2      A3          3      D2          0

Variables:
B1          1.76
B2          1.09
B3          1.09
B4          1.09
D1         -120.
D2        120.00001
A1        109.4712
A2        109.47121
A3        109.47121

-----
! Optimized Parameters !
! (Angstroms and Degrees) !
-----
! Name  Definition          Value          Derivative Info.
! -----
! R1    R(1,2)              1.7889        -DE/DX =    -0.0001
! -----
! R2    R(1,3)              1.0782        -DE/DX =      0.
! -----
! R3    R(1,4)              1.0782        -DE/DX =      0.
! -----
! R4    R(1,5)              1.0782        -DE/DX =      0.
! -----
! A1    A(2,1,3)            108.2543      -DE/DX =      0.
! -----
! A2    A(2,1,4)            108.2543      -DE/DX =      0.
! -----
! A3    A(2,1,5)            108.2543      -DE/DX =      0.
! -----
! A4    A(3,1,4)            110.6603      -DE/DX =      0.
! -----
! A5    A(3,1,5)            110.6603      -DE/DX =      0.
! -----
! A6    A(4,1,5)            110.6603      -DE/DX =      0.
! -----

```

Input orientation:

Center Number	Atomic Number	Atomic Type	Coordinates (Angstroms)		
			X	Y	Z
1	6	0	0.000000	0.000000	-1.130669
2	17	0	0.000000	0.000000	0.658187
3	1	0	1.023921	0.000000	-1.468391
4	1	0	-0.511960	0.886742	-1.468391
5	1	0	-0.511961	-0.886741	-1.468391

Distance matrix (angstroms):

		1	2	3	4	5
1	C	0.000000				
2	Cl	1.788856	0.000000			
3	H	1.078179	2.360244	0.000000		
4	H	1.078179	2.360244	1.773483	0.000000	
5	H	1.078179	2.360244	1.773483	1.773483	0.000000

Stoichiometry CH₃Cl

Framework group C_{3v}[C₃(CCl), 3SGV(H)]

Deg. of freedom 3

Full point group C_{3v} NOp 6

Largest Abelian subgroup CS NOp 2

Largest concise Abelian subgroup CS NOp 2

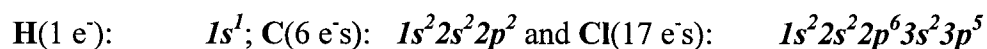
The character table of molecules with symmetry elements of C_{3v} group is given in

Table 3.2

Table 3.2: Character table of C_{3v} symmetry group

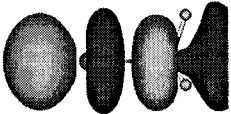
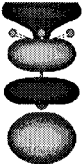

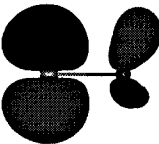



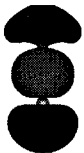

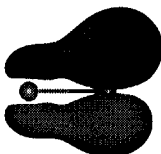


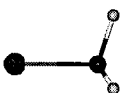


C_{3v}	E	$2C_3(z)$	$3\sigma_v$	
A_1	1	1	1	z
A_2	1	1	-1	R_z
E	2	-1	0	$(x,y); (R_x,R_y)$

The CH₃Cl molecule has a total of 26 electrons, which are distributed in the ground state among the participated atoms with the electronic configurations as follows:



The shape and symmetrical orientation along the X -, Y -, and Z -axis of calculated MOs with large contributions of chlorine AOs are presented in Table 3.3.

Table 3.3: Shape and symmetry of molecular orbitals of CH₃Cl

MOs	X (YZ)	Y (XZ)	Z (XY)	Symmetry
$8a_1$				σ -type
$3e^4$				π -type
$7a_1^2$				σ -type
$2e^4$				π -type
$1a_1^2$				σ -type

The MO energies with different models of calculation are presented in Table 3.4. The chlorine AO populations (molecular orbital coefficients) are presented in Table 3.5 for calculation method using 3-21G basis set.

Table 3.4: Molecular orbital energy of the CH₃Cl molecule

MOs	<i>Ab Initio</i> Calculation (eV)		
	3-21G	6-31G(d)	6-311G(d,p)
$8a_1$	5.491801398	5.274654558	1.797311874
$3e^4$	-11.90579658	-11.82878836	-11.88048999
$7a_1^2$	-14.59591394	-14.81306078	-14.85442208
$2e^4$	-17.14888593	-16.95486877	-16.94398422
$1a_1^2$	-2832.406775	-2852.055843	-2852.418299

Table 3.5: Calculated population coefficients of MOs using 3-21G basis set

MOs	Chlorine AOs	Symmetry
$8a_1$	(-0.75395) Cl $4s$ + (-0.32852) Cl $3p_z$	σ -type
$3e$	(0.58841) Cl $3p_y$ + (-0.26971) Cl $2p_y$	π_y -type
$3e$	(0.58841) Cl $3p_x$ + (-0.26971) Cl $2p_x$	π_x -type
$7a_1$	(0.47976) Cl $3p_z$ + (-0.22393) Cl $2p_z$ + (-0.10600) Cl $3s$	σ -type
$2e$	(0.18036) Cl $3p_x$	π_x -type
$2e$	(0.18036) Cl $3p_y$	π_y -type
$1a_1$	(0.9859) Cl $1s$	σ -type

3.6. Interpretation of PXES experimental data of CH₃Cl

Figure 3.2 shows a measured absorption spectrum [2,10] of CH₃Cl in the vicinity of the Cl *K* edge and a Cl *K-V* valence-electron fluorescence spectrum taken with an incident photon energy of 2880 eV, well above the Cl *1s* threshold. Also shown in Fig. 3.2 is an energy level diagram for molecular orbitals involved in electronic transitions. The experimental spectra are aligned with the energy level diagram. It can be seen easily that absorption spectrum maps out the unoccupied states, while the emission spectrum maps out the occupied valence levels of the molecule.

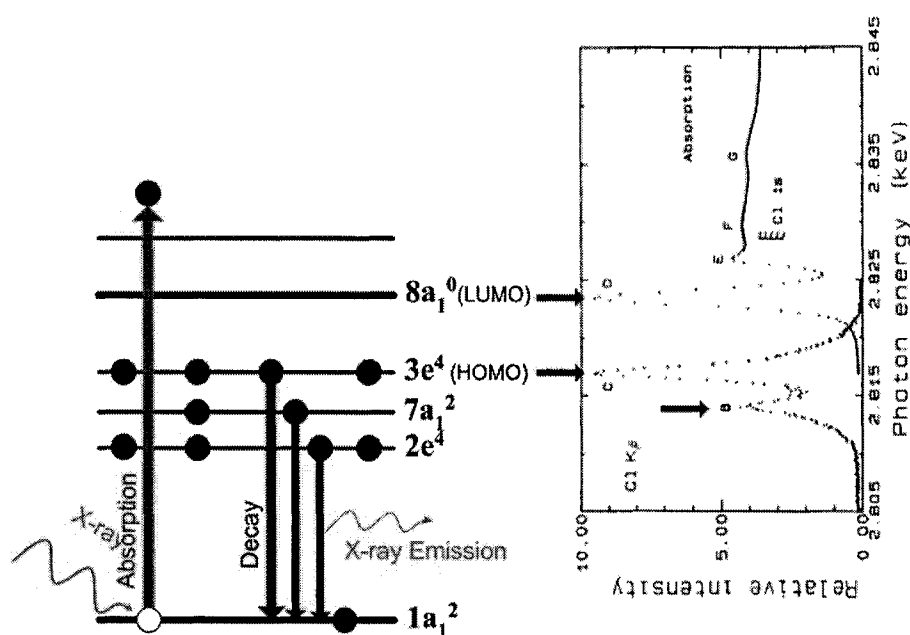


Figure 3.2: XAS and NXES spectra of CH₃Cl. The x-ray emission spectrum was measured at photon energy of 2880 eV. On the left side is an energy level diagram of MOs involved in electronic transitions.

Peak labels and energies are listed in Table 3.6 together with their assignment. The peak energies are calculated by $h\nu = E_p - E_{1s}$, where E_p is the energy of an atomic-*p*-character

molecular orbitals involved in electronic transitions, and E_{1s} is energy of molecular orbital with Cl $1s$ -character.

Table 3.6: Peak energies and assignment.

Peak	$E_{\text{Calculated}}$ (eV)			$E_{\text{Experiment}}$ (eV) [10]	Assignment
	3-21G	6-31G(d)	6-311G(d,p)		
D	2837.8986	2857.3305	2854.2156	2823.4	$1a_1 \rightarrow 8a_1$
C	2820.501	2840.2271	2840.5378	2817.1	$3e \rightarrow 1a_1$
B	2817.8109	2837.2428	2837.5639	2814.1	$7a_1 \rightarrow 1a_1$
B	2815.2579	2835.101	2835.4743	2814.1	$2e \rightarrow 1a_1$

As shown in Table 3.6, theoretical calculation of molecular orbital energy for the CH_3Cl molecule in ground state with different models of *ab initio* method does not give a good description for the experimental peak positions. More sophisticated theories may need to be employed [2]. However, the shape and symmetrical characteristics of calculated molecular orbitals can be used for a qualitative interpretation of experimental XES spectra. Specifically, the peak assignment has been made based on the relative positions of energy levels on the energy diagram (see Fig. 3.2) as well as on the symmetry properties of the MOs involved (Tables 3.3).

The symmetry of MOs as shown in Tables 3.3 is also quite useful for describing the principle of polarized x-ray emission spectroscopic technique. Feature *D* on the XAS spectrum is attributed to the excitation of Cl $1s$ (CH_3Cl $1a_1$) to the $8a_1$ anti-bonding orbital. The Cl K - V fluorescence in Fig. 3.2 results from electrons in valence MO's filling

the Cl $1s$ -hole produced by absorption of the incident radiation. Only MO's with significant atomic Cl $3p$ -character contribute to the XES spectrum because of dipole selection rules (hence, Cl $3p$ - but not Cl $3s$ -character) and because the K -hole is localized on the Cl atom (hence Cl $3p$ - but not carbon $2p$ -character) [2]. As shown in Table 3.5, the relevant valence MO's (i.e, with Cl $3p$ -character) of CH_3Cl are the three outer-most filled orbitals: $3e$, $7a_1$, and $2e$, in order of increasing binding energy. There are only two peaks observed on the XES spectrum of CH_3Cl because the $7a_1$ and $2e$ orbitals are unresolved in peak B [2]. With 2880 eV excitation, as shown from the emission spectrum in Fig. 3.2, no detectable change with fluorescence-polarization angle was observed [2,10]. On the other hand, using near-threshold excitation at 2823.4 eV, centered on feature D of the absorption spectrum in Fig. 3.2, a big difference in behavior of K - V spectra as a function of the emission polarization angle is obtained (Figure 3.3). Specifically, the ratio of relative intensities of peak B to C for the measurement of polarization parallel to the polarization of incident beam is larger than that for the perpendicular direction measurement.

Qualitatively, the PXES results of Fig. 3.3 can be understood by realizing that CH_3Cl molecules excited with incident energies on feature D ($1a_1 \rightarrow 8a_1$) will preferentially have their molecular symmetry axes (along the C-Cl bond) aligned with the direction of the synchrotron radiation polarization (as shown on the left hand side of Fig. 3.3). This alignment is retained in the subsequent K - V radiative decay because emission occurs so rapidly ($\approx 10^{-14}$ s) that the molecules remain essentially fixed in space throughout the absorption and emission processes [2]. Consequently, because of cylindrical symmetry (σ -type) of the $7a_1$ MO about molecular axis, as shown graphically in Table 3.3, emission

from the $7a_1 \rightarrow 1a_1$ transition, which contributes to $K-V$ peak B, is also polarized along the molecular symmetry axis. X-rays emitted from this transition, therefore will be polarized parallel to the synchrotron radiation polarization. On the other hand, emission by transitions from $3e$ and $2e$, which have symmetry of π -type, to $1a_1$ ($K-V$ peaks C and B, respectively) is polarized perpendicular to the molecular symmetry axis and thus produce x rays polarized perpendicular to the synchrotron radiation polarization.

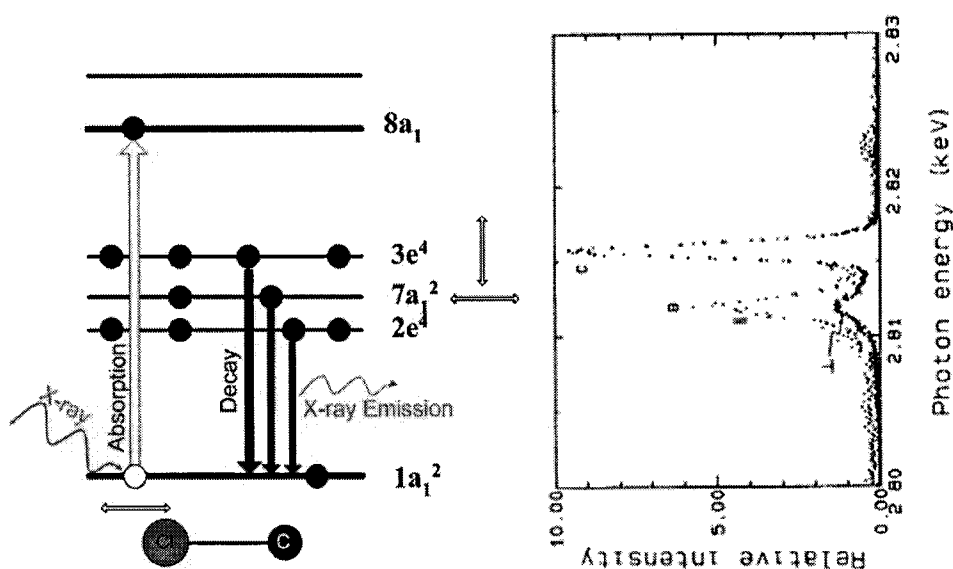


Figure 3.3: Resonant XES spectra of CH_3Cl . The x-ray emission spectrum was measured at photon energy of 2823.4 eV. On the left side is energy level diagram of MOS involved in electronic transitions.

The significant difference in the B -to- C peak ratios of x-ray emission spectra of CH_3Cl in the two orthogonal polarizations demonstrates anisotropy in polarization of molecular x-ray emission that depends on symmetry of the involved molecular orbitals and forms the basis for PXES as a technique to study electronic structure of molecules.

CHAPTER 4

DEVELOPMENT OF THE X-RAY EMISSION SPECTROMETER

X-ray emission spectra excited by tunable monochromatic radiation are valuable for the study of atoms and molecules. In general, an efficient, high-resolution secondary x-ray spectrometer is critical to studies of x-ray emission spectra. Additionally, core-level polarized x-ray emission measurements require [10]:

1. An intense source of x rays. In addition, highly polarized incident radiation is desired because it enhances effects observed by PXES.
2. An efficient, high-resolution primary monochromator.
3. An efficient, high-resolution secondary x-ray spectrometer.
4. Polarization sensitivity of the secondary spectrometer.

These requirements for experiments are realized by development of a polarization-sensitive x-ray emission spectrometer at beamline 9.3.1 of the ALS [20].

4.1. XES Spectrometer

In Figure 4.1 is schematic diagram of the x-ray emission spectrometer, and the picture of the spectrometer at beamline 9.3.1 is shown in Figure 4.2.

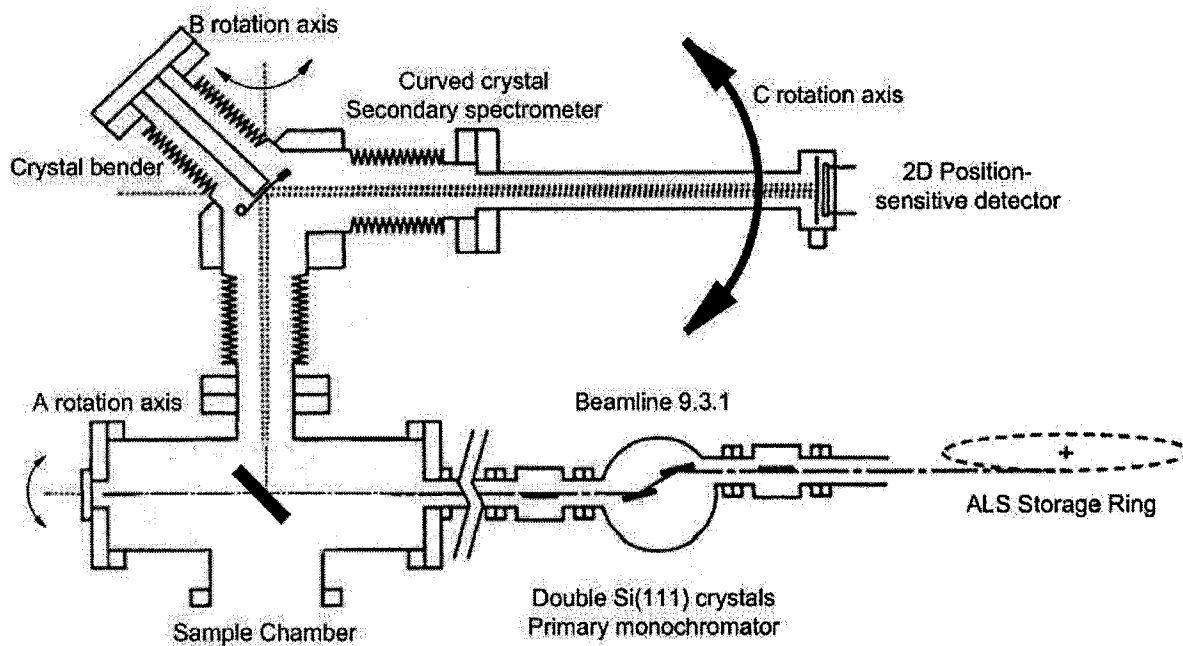


Figure 4.1: Schematic diagram of x-ray emission spectrometer (XES)

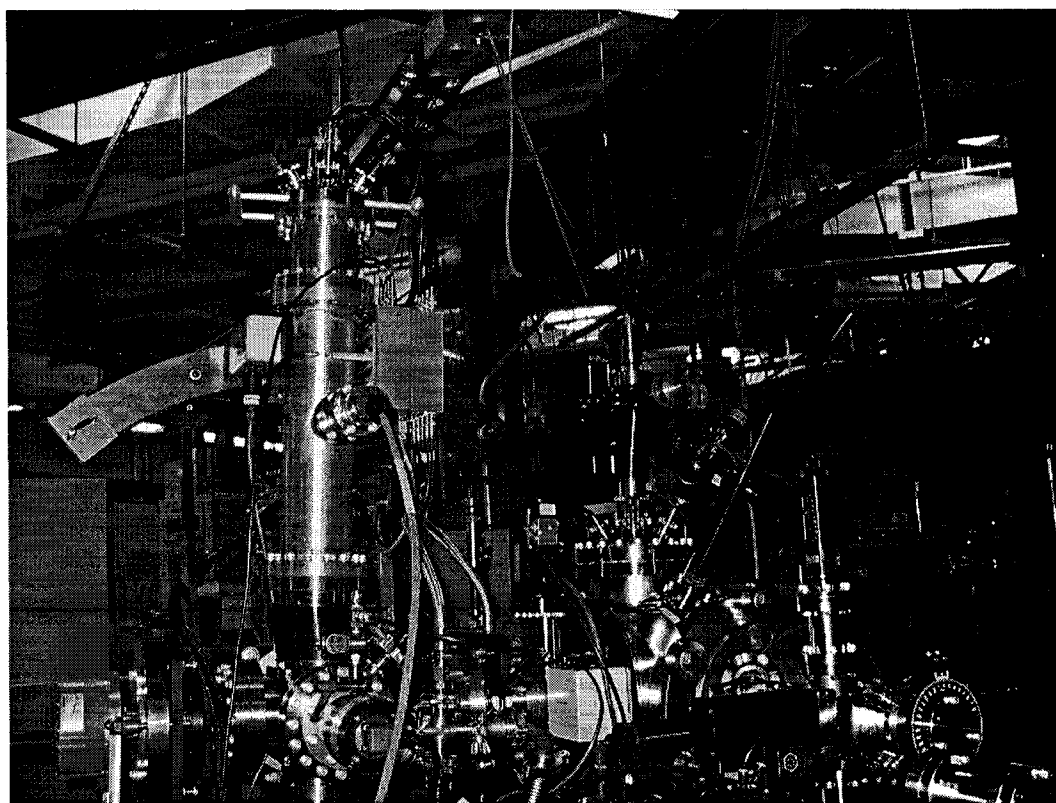


Figure 4.2: X-ray emission spectrometer at beamline 9.3.1, ALS.

Mechanically, there are two main parts that build up the endstation: a sample chamber and a secondary spectrometer with crystal bender and detecting system. Samples of solid powder and crystal are mounted on a sample holder and introduced to the sample chamber, where the interaction with incident radiation occurs. The crystal bender is situated inside a separated chamber mounted to the spectrometer by a frame with a bellows in between, while the detector is mounted on a supporting arm, which is also joined with the crystal chamber by a bellows. While maintaining high vacuum ($<10^{-7}$ torr), the construction of the endstation allows continuous rotation of the main parts, individually or in combination, about three axes A, B, and C as shown in Fig. 4.1. The whole chamber can be rotated about axis A, the propagation direction of the incident beam, thus angular dependence measurements with respect to the polarization of the incident radiation can be performed. The secondary spectrometer can be rotated about axis B perpendicular to the propagation direction of the incident beam, thus polarization dependence of x-ray emission can be obtained. At any position of the secondary spectrometer, the supporting arm for the detector can be rotated about axis C, centered at the crystal chamber and perpendicular to axis B, thus different energy ranges of x-ray emission can be detected. Finally, the crystal bender chamber can be adjusted by rotating about axis C. The bellows allows small adjustments in relative orientations between crystal and detector, and therefore optimal focusing of x-rays onto the detector can be achieved. The system construction therefore allows high-resolution measurements of x-ray emission with energy, angle and polarization dependence.

High vacuum is maintained by two turbo pumps, one each mounted to the sample chamber and the secondary spectrometer. Vacuum valves have been included that allow

separation between the whole chamber and the beamline as well as between the secondary spectrometer and the sample chamber.

The incident beam direction and polarization vector lie in the horizontal plane (plane of the storage ring) for the PXES measurements. Incident x-rays from the beamline go into the spectrometer through the sample chamber, where x-rays interact with the sample. X-ray fluorescence emitted normal to this plane by excited or ionized molecules passes into the secondary spectrometer for energy analysis. The secondary spectrometer is of Johann geometry, with the dispersing crystal and x-ray detector situated on a Rowland circle of variable radius, with the crystal-to-detector distance fixed at nominally 1 m [48]. The schematic diagram of the focusing geometry is given in Figure 4.3.

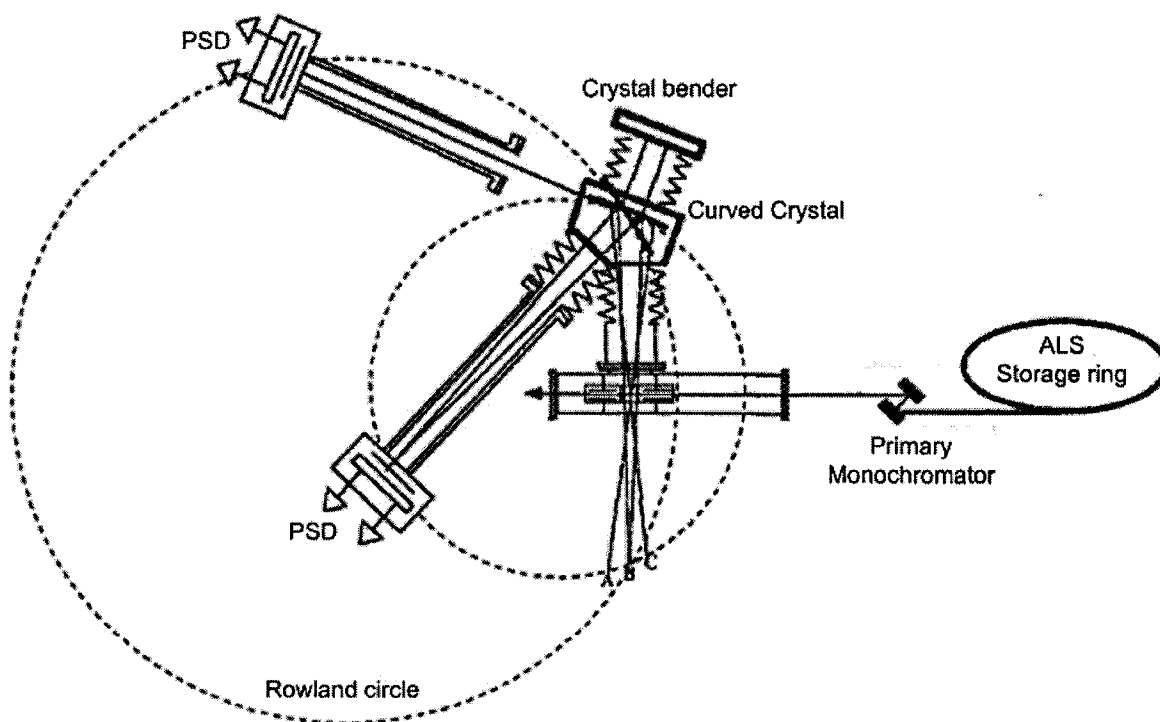


Figure 4.3: Schematic diagram of a variable Rowland circle spectrometer with fixed chord length for both sample-crystal and crystal-detector.

The target-sample is positioned inside the Rowland circle (off-circle source position) by making the target-crystal distance shorter than the crystal-detector distance. This configuration allows collecting multiple wavelengths by the detector and reducing sensitivity to alignment of the primary beam with respect to the secondary spectrometer [48]. As in the primary monochromator of the beamline, a Si (111) crystal is used to diffract the x-rays for experiments with x-ray energies around the Cl *K*-edge fluorescence (≈ 2.8 keV). This crystal is cylindrically curved by a crystal-bending device [49], and the radius is adjusted externally to optimize the focus and thus the energy resolution of the spectrometer. Polarization selectivity of the secondary spectrometer is provided by the use of a Si (111) crystal at a Bragg angle corresponding with the desired photon energy (for example, for Cl *K-V* emission measurement, the Bragg angle is 44.6°). The polarization component of the x-ray fluorescence to be measured (parallel to the crystal surface) is thus diffracted more efficiently by at least a factor of 10^3 relative to the orthogonal component (out of the plane of the crystal surface) [48]. Polarization selection is accomplished by orienting the dispersion plane of the secondary spectrometer either parallel or perpendicular to the propagation vector of the synchrotron radiation, ensuring that fluorescence from the sample polarized parallel or perpendicular, respectively, to the incident polarization vector is primarily detected. Thus, a rotation of the secondary spectrometer by 90° about the vertical axis (B-axis) of Fig. 4.1 suffices to measure orthogonal polarizations of x-ray emission. The diffracted x-rays are detected by a two-dimensional position-sensitive detector (PSD). Operation with the PSD allows a complete x-ray emission spectrum (≈ 50 eV wide) to be accumulated simultaneously.

4.2. Sample holder

A holder for solid samples has been designed and made from aluminum. The design and picture of the sample holder is presented in Figure 4.4.

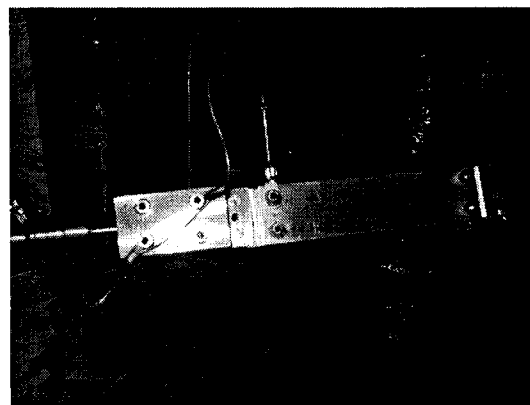
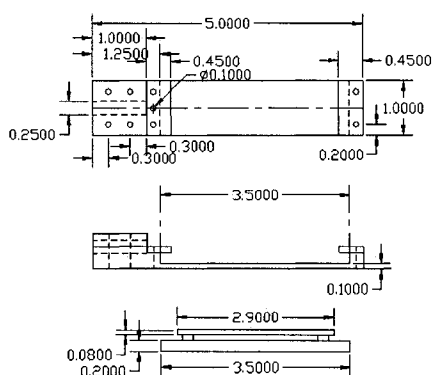


Figure 4.4: Design and picture of the holder for solid samples

Solid powder samples are mounted on an aluminum plate by carbon tape that ensures an electrical connection between the samples and the plate. This plate is mounted isolated on a substrate by using ceramic rings, washers and wire-connected to the outside electrode with a vacuum feedthrough for measurements of photo-current from samples created during interaction with incident radiation. The substrate slides in and out through a slot-form of the sample holder for mounting and replacing samples. The sample holder is mounted on a special manipulation table that allows movement of the sample in X, Y and Z directions as well as rotation of 360° . A 1-mm hole on the sample holder helps to define the position of the sample holder relative to the incident beam and thus helps to align the chamber on the beamline.

4.3. Detector system

4.3.a. Components of the detector system

The detector system consists of an open-face microchannel plate/resistive anode encoder (MCP/RAE model 3395A) sensor mounted in a vacuum chamber, a position analyzer 10-bit digitized output (model 2401B) from Quantar Technology Inc. with the preamp, an auxiliary HV bias power supply and voltage divider network, an oscilloscope for real-time monitoring and a computer-based digital data acquisition system. Figure 4.5 presents the schematic diagram of the detecting system.

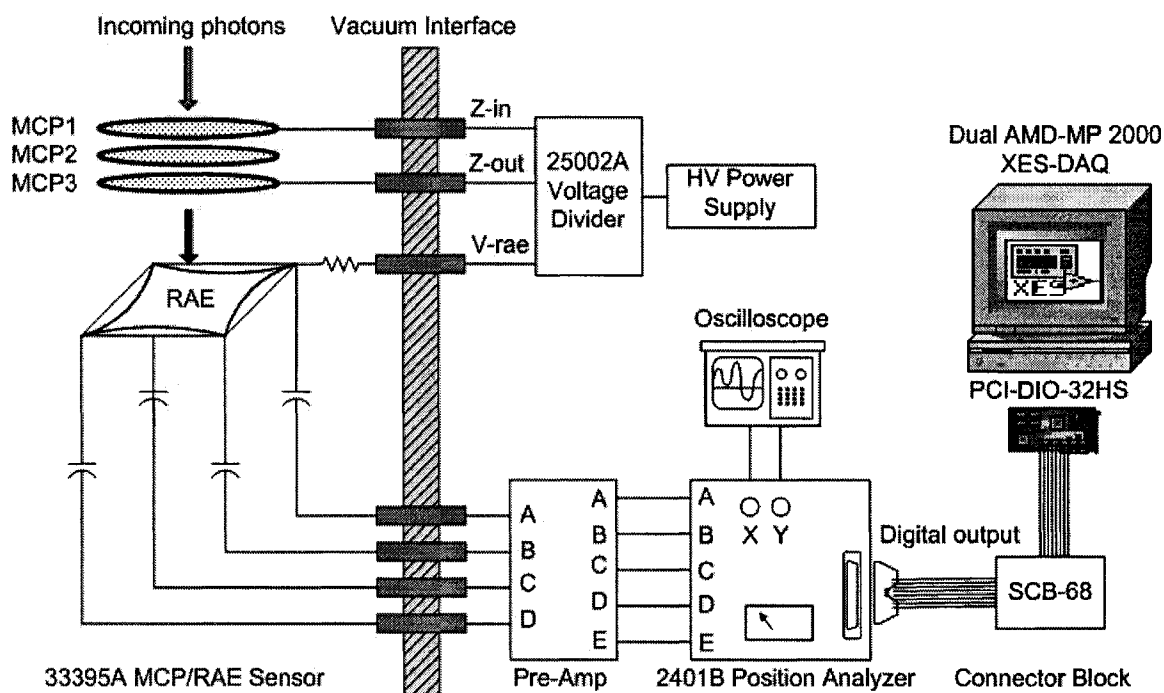


Figure 4.5: Schematic diagram of position sensitive detector and data acquisition system

The MCP/RAE sensor head is of high spatial-resolution version and includes 3 MCPs (rimless type) with circular active diameters of 40 mm. A MCP is an approximately 1mm thick plate comprised of a honeycomb of electron multiplying channels. Since each

channel is about 25 μm in diameter with center-to-center spacing of 32 μm , this gives approximately 2.5×10^6 channels per plate (or 1600 channels in each directions X and Y). The surface of input MCP is coated with 300 nm CsI that make it more efficient than a basic MCP in the soft x-ray region by improving the efficiency up to an order of magnitude [48]. The MCP/RAE components are held in place on a spring-loaded assembly that is screwed into a 2.9'' diameter ceramic base-plate containing all electrical leads (Figure 4.6). The sensor leads are capacitively decoupled and shielded, which is necessary to prevent arcing due to the high voltages applied. The sensor head is mounted electrically isolated on an aluminum base-plate by four supporting pillars. This plate is mounted on a 6'' multiport Del-Seal-type flange. The hardware is installed on the arm of the spectrometer chamber under high vacuum.

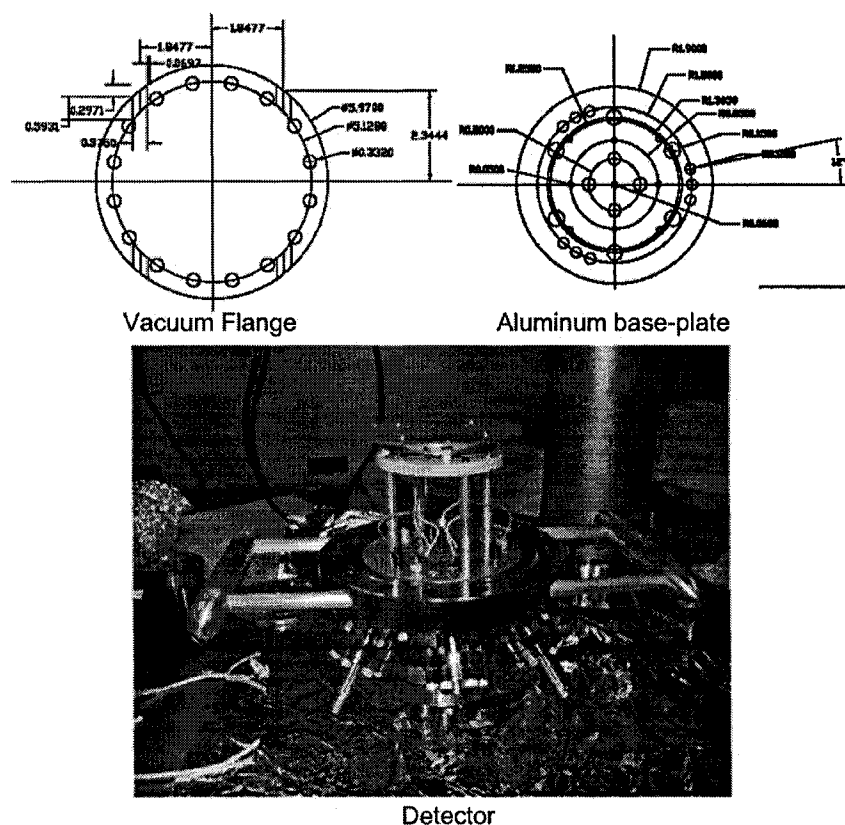


Figure 4.6: Detector head and supporting flange

The MCPs and RAE are biased with operating voltage of 700-1000 V per MCP by an HV power supply through a 25002A HV bias divider. The four signal-leads exit the chamber and interfaces with a 2401 charge-sensitive Preamplifier/shaper module that amplifies the signals and converts the low-level pulses to high-level shaped bipolar pulses for processing by the 2401B position analyzer. A 22-lead custom-made cable connects position analyzer to the external computer and feeds the digital output of position analyzer via a SCB-68 connector block into a digital input card (PCI-DIO-32HS from National Instrument) located inside a dual AMD Athlon MP-2000 PC computer. Software written in LabVIEW for Windows 2000 is used for setting up communication between position analyzer and external computer and for data acquisition.

4.3.b. Principle of operation

In operation, single incoming events (photons) impact the MCP surface and result in an electron cascade. Approximately 5×10^7 electron gains are obtained with present type and configuration of MCP's under operating bias voltage of 2.5 kV [50]. The MCP's operate in a gain-saturated mode to ensure a relatively constant gain from event-to-event to optimize position determination. The resulting charge packet from the MCP stage is electrostatically focused on the charge-division anode that results in a measurable pulse of charge on the resistive anode. This charge is divided among the four corner collection electrodes (A, B, C and D) of the resistive anode in proportion to the spatial position of incidence. Four pulse signals are processed by separate charge-sensitive preamplifiers, shaper amplifiers and discriminators. The X and Y spatial coordinates of each detected event, corresponding to a single incoming photon, are then computed by the position analyzer from the ratio of charge pulse amplitudes.

$$X = \frac{B+C}{A+B+C+D} \quad \text{and} \quad Y = \frac{A+B}{A+B+C+D} \quad (4.1)$$

The X and Y position is output in analog format for real-time display on an analog CRT XY monitor (such as a 2-channel oscilloscope operated in X-Y mode). A fast (130 MHz clock rate) analog-to-digital (ADC) converter of Wilkinson type provides two sampled 10-bit digital representations (digital bit numbers in the form of TTL-level, positive-true pulses) of the analog position voltage on each axis. The dead-time of the system with 10-bit ADC is about 10 μ sec. These signals can be then read directly by a computerized data system.

4.3.c. Computerized data collection system

The digital format of X and Y positions are output on a 50-pin Amphenol ribbon-type connector at the rear of the position analyzer box. Pins 1-10 output the 10 bits of Y axis position information while pins 11-20 output the available 10 bits of X axis position information.

The PCI-DIO-32HS digital input card is used to read and collect data from position analyzer with the data acquisition software. The PCI-DIO-32HS device is high-speed, 32 bit, parallel, digital I/O interface for PC computer with a PCI expansion slot [51]. It incorporates the National Instrument DAQ-DIO ASIC, specifically designed to deliver high performance on plug-in DIO devices. The PCI-DIO-32HS device performs unstrobed I/O, pattern I/O, and handshaking at speeds up to 20 MHz, or 80 Mbytes/s for 32-bit transfers. The 32 digital I/O lines are divided into four 8-bit ports. For the present application, where it is required to read two 10-bit inputs of X and Y positions

simultaneously, the ports are configured into two 16-bit groups, ports 0-1 for Y digital signals and ports 2-3 for X digital signals:

Port0: reads first 5 digits of Y-position

Port1: reads last 5 digits of Y-position

Port2: reads first 5 digits of X-position

Port3: reads last 5 digits of X-position.

The digital input lines for each port are then assigned correspondently for X and Y signals through connectors of SCB-68 connector block [52] and by parameter setup in software.

4.3.d. Data acquisition software (XESDAQ)

Software design for the detector system of the XES endstation is governed by several factors, such as the specifications of actual XES experiments and capabilities of hardware. We used LabVIEW Graphical Programming Language of National Instrument Inc.[53] under Windows 2000 (Microsoft Corp.) to develop the data acquisition software for the detector system of the XES endstation. LabVIEW delivers a powerful graphical development environment for signal acquisition, measurement analysis, and data presentation, while giving the flexibility of a programming language without the complexity of traditional development tools. The Windows driver for the plug-in digital input card is provided by NI-DAQ (a collection of driver software for Windows, also from National Instrument Inc.), that inherently supports and simplifies the software development in LabVIEW.

High-speed performance of PCI-DIO-32HS device allows performing digital input continuously. Thus a continuous data acquisition mode has been employed that ensure

that all output data from position analyzer is transferred to computer for processing. This mode of operation takes full advantage of the capabilities of a dual AMD processor computer by parallel-programming algorithms employed in software and inherent parallel-processing support of LabVIEW.

In x-ray emission measurement, x-rays emitted from the sample are diffracted at Bragg angles by the curved crystal of the secondary spectrometer and disperse on the plane of the detector. Position of incoming photon on the surface (specifically, on the dispersive axis, usually Y -axis) of the detector depends on photon energy (hence Y -axis is called energy dispersive axis). Single events of x-ray photon are detected and accumulated during a period of time and images are developed from the integration of these single events. A two-dimensional image of the detector provides a position distribution of the number of x-ray photons (x-ray emission intensity) and therefore photon energy-dependent spectra are obtained along the energy dispersive axis.

The position distribution of the number of photons can be represented by a two-dimensional $Z[x,y]$ -matrix, where x and y are the position (coordinate), where photons hit the detector, provided by the position analyzer on the X and Y -axis, respectively, and Z is the number (count) of photon. Since there are $2^{10} = 1024$ (10-bit) of X positions (channel X) and $2^{10} = 1024$ (10-bit) of Y positions (channel Y), the Z -matrix is a $[1024 \times 1024]$ matrix with $(2^{10} \times 2^{10}) = 1048576$ elements. The Z -value of each element represents for photon intensity at corresponding position (x,y) . In the data acquisition process, the accumulation procedure of Z -matrix starts with initialization in which all element of Z -matrix are set to zero. Every single event of photon is captured by the detector and processed by the position analyzer that gives a pair of X and Y digital positions. The

external computer under software control reads the digital X and Y data, converts to x and y positions and increases the Z -value of the corresponding (x,y) element of Z -matrix by 1 (add-one algorithm). Accumulated Z -values after a period of time are displayed in a 2-dimensional graph that represents the image of the detector.

The program to realize the data acquisition process above therefore has two main functions: Reading (acquisition) digital data from position analyzer and, consequently, processing (converting and counting) data. In Figure 4.7 is the flow chart diagram of the XESDAQ software that includes main program and functions. Each function (procedure) is a subroutine, also written in LabVIEW and called a VI block that performs a specific task (operation) following the command (control) of the main program. The arrows show the order of operations in the main program.

The main program can be divided in two parts: On the left hand side is flow chart of the reading process, in which the ports of the PCI-DIO-32HS digital input card are configured to read all digital data from output of 2401B using continuous mode. Acquired data is then buffered in internal memory of the computer. On the right hand side is data processing and counting process, in which data from buffer is converted to (x,y) position and the value of $Z(x,y)$ element is counted by 1.

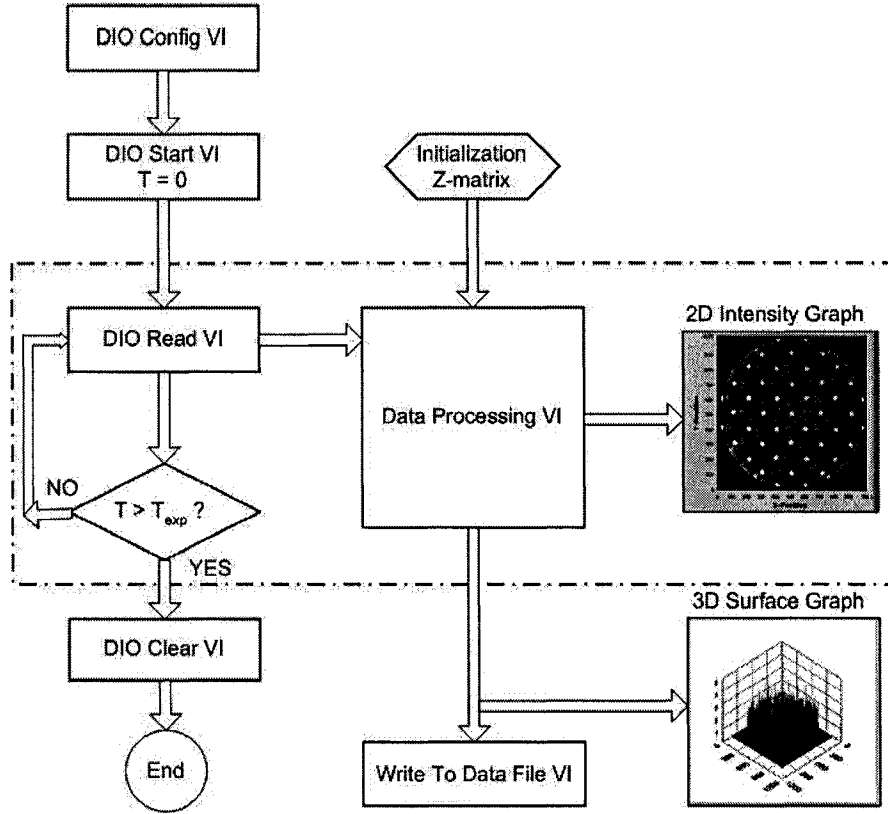


Figure 4.7: Flow chart diagram of the data acquisition software XESDAQ for PXES

The flow chart of the data processing block is given in Figure 4.8. Every reading circle gives a 1-D array of data converted to decimal base from digital data (binary base) of 4 ports of digital input card. The converted data is arranged by the order of reading and accommodated in buffer with the same order. The data processing block reads data from the buffer by its order and converts to x - and y -value as follows:

$$x = X_{0-4} + 2^5 * X_{5-9}, \text{ and } y = Y_{0-4} + 2^5 * Y_{5-9} \quad (4.2)$$

where, $Y_{0-4}, Y_{5-9}, X_{0-4}$, and X_{5-9} are the data read from ports 0, 1, 2, and 3 of the input card, respectively.

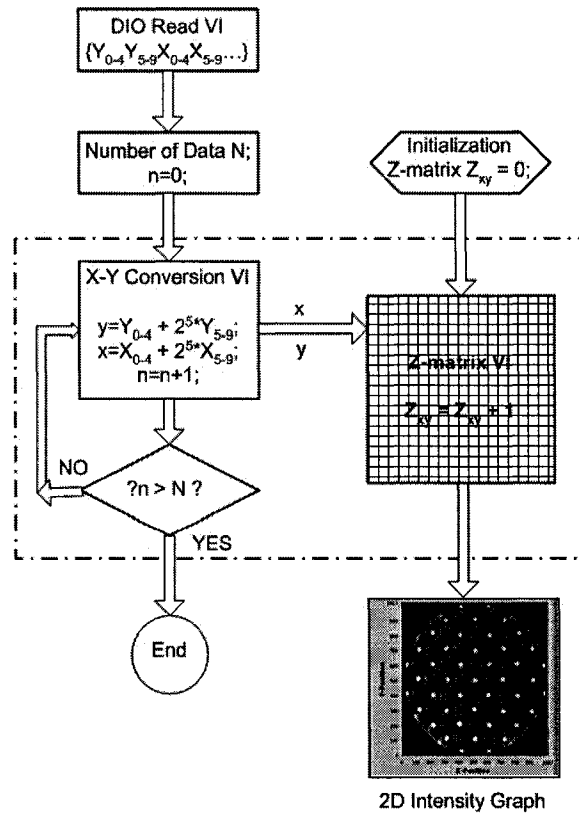


Figure 4.8: Flow chart diagram of “Data processing VI” block

Using data buffering allows two processes to occur virtually parallel. After filling the buffer with data, the ports of the digital input card are ready for reading of new data, while contents of the buffer are read by the data processing block that makes the buffer empty and ready for new data and so on. The “new” Z-matrix is updated for every processed pair of x - and y -values. When all buffered data of a reading circle (loop) is processed, the Z-matrix is displayed in 2-D graph on the monitor of the computer. A near “real-time” monitoring of detection therefore can be observed.

User-defined period of time for measurement t_{exp} is only input parameter for software. When the program starts, it automatically establishes digital port configuration and communication with the position analyzer and performs fast, continuous data acquisition

and computation. The near “real-time” 2-D image is observed on the display of the computer together with running time, remaining time and total count number as well as count rate. At the end of measured time, accumulated data is save to data file in compatible formats for data analyzing software like ASCII, Excel, MathLab or binary file. The final data is also presented in a 3-D surface graph that can be manipulated to obtain the profile of image or spectrum.

CHAPTER 5

PERFORMANCE OF THE SPECTROMETER AND DETECTOR SYSTEM

A series of testing procedures have been performed to test the operational functions of the developed software and performance of the detector system. Spatial resolution of the detector has been tested and calibrated with the resolution of the image obtained by the data acquisition software. The detector system is then used for initial performance tests of the x-ray emission spectrometer by studying a solid powder sample of potassium chloride. An effective detectable energy range and spectral resolution of the detector has been obtained for the photon energy range in the vicinity of Cl *K* edge. An initial test for the polarization-sensitivity of the spectrometer has also been performed.

5.1. Testing detector with a UV light source and performance

The detector system including all electronics and data acquisition software has been tested by using a testing stand and a UV light source. A stainless steel mask has been machined with linear arrays of 0.6 mm diameter holes with center-to-center spacing of 5.0 mm. This mask is mounted in front of the detector head for the linearity testing. The UV light source is provided by a Pen-Ray mercury lamp with the wavelength of 254 nm. In Figure 5.1 is the image of the mask with testing time of $t_{\text{exp}} = 30$ sec and operating HV of 2.5 kV.

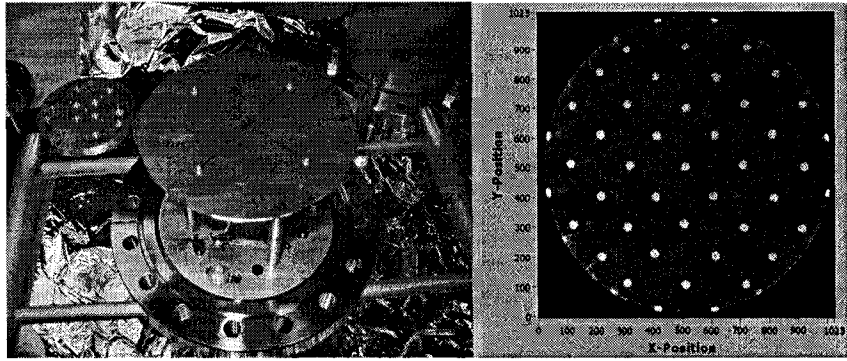


Figure 5.1: Image of a linear testing mask recorded with a UV lamp

* **Linearity:** The image shows the perfect linearity of the detector. Distortion at the edge of some holes is attributed to misalignment of the UV lamp with respect to the center of the detector as well as unequal distances from the point-type light source to the holes of the mask. No distortion on the edge of the active surface of the detector has been observed, thus the effectively detectable area of the detector could be widely expanded.

* **Spatial resolution:** The spatial resolution of the detector is about $1/400$ of active diameter, i.e about 0.1 mm or 2.6 channels. The recorded image shows each hole represented by approximately 20 channels equally in both X and Y axis. Since each channel of axis X or Y represents for about 40 μm of the active surface of the detector, the diameter of the image of the holes is estimated about 0.8 mm. The difference between the actual and recorded diameter of the holes is attributed to the scattering of light on the edge of the holes that creates the diffusion of light. The distance between the mask and active surface of the detector also contributes to the light diffusion that creates background count signals in the space between holes as seen in Figure 5.1.

* **Accuracy:** The accurate reproduction of the image of the mask itself has shown the accuracy in term of functional operations (algorithm) and performance of the data acquisition software and electronics components of the detector system.

* Speed of computation: In operation, the detector system under control of software performs a fast data acquisition, data processing, and provides a near “real-time” monitoring of the positions of events on the surface of the detector.

* Count rate: While there is no light, the system gives a background less than 10 counts/sec. For perfectly time-periodic input counts, the 10 μ sec dead time of the position analyzer with 10-bit digital output translates to a maximum output count rate of 1×10^5 counts/sec [50]. The computerized data collection system with processing software has been tested with the rate up to up to 3×10^5 counts/sec without any data lost. Although this count rate can also be increased by changing the size of the memory buffer, it certainly suffices for the current application of x-ray emission measurements, where the count rate is about 100 counts/sec, since the achieved performance of the computer and software is already higher than the capability of the hardware. We, therefore, believe that the performance of the data acquisition system is quite suitable for actual experiments of XES.

5.2. XAS measurement of KCl

Samples of solid powder of potassium chloride KCl have been used to test the performance of the x-ray spectrometer and detector system with x-rays from beamline. First, chlorine x-ray absorption spectrum has been measured on the sample to calibrate the photon energy of beamline. In Figure 5.2 is XAS spectrum of KCl obtained in the photon energy range of 2815-2885 eV, near the absorption threshold of chlorine, by measuring the photo-current from the sample (total-electron-yield). The main peak on the present XAS spectrum is sharp with an approximate FWHM of about 2.25 eV and is

identified at 2826.7 eV. This peak is attributed to the transition of Cl *1s* excited to continuum conduction band [54]. Experimental chlorine fluorescence-yield measurement of KCl [55], shows the main peak at 2824.4 eV. Therefore, a shift of -2.3 eV has been applied to photon energy of the beamline for all measurements in the vicinity of Cl *K*-edge.

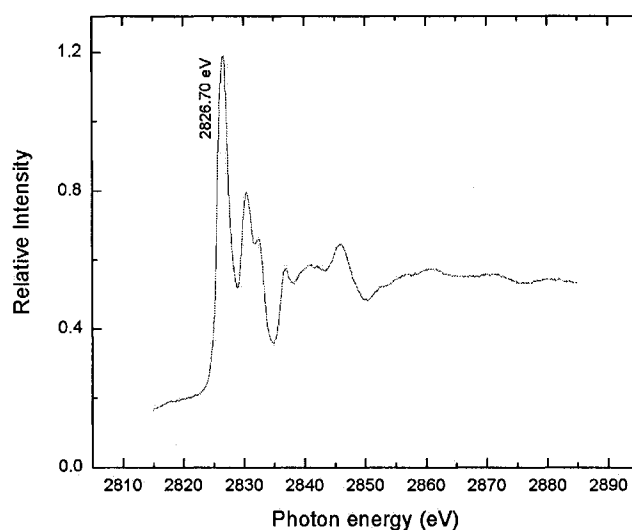


Figure 5.2: X-ray chlorine absorption spectrum of KCl

5.3. Testing the detector with beamline x-rays and performance of the spectrometer

* Alignment of the spectrometer:

Alignment of the secondary spectrometer and the detector with respect to the beamline direction is critical for the position-sensitive measurements of x-ray emission. A wafer of Si (111) is mounted on the sample holder and used to align the secondary spectrometer. The spectrometer is set at the Bragg angle of 45° for alignment. Thus the sample holder is set at 45° , the detector arm is set at 0° and the detector is set at position parallel with respect to the beam propagation direction (position in Figure 4.1). After

fixing the photon energy at 2796.07 eV (corresponding to the Bragg angle of 45^0 for Si (111)), the crystal-bender chamber orientation and radius of curved crystal are adjusted to track the light spot and to obtain the best focusing on the surface of the detector. The “real-time” digital data acquisition system as well as an analog X-Y oscilloscope has been used for monitoring the alignment by observing images of the detector. The use of Si (111) wafer simplifies the spectrometer configuration setup (45^0 configuration). However, much care should be taken since strong intensity of light diffracted from Si (111) wafer could damage the active surface of the detector. The enter slits of the spectrometer have been used to decrease the size of the incident beam to minimal (about 0.5 mm). By controlling the biased voltages for the MCPs of the detector, the electron gain could be controlled to an acceptable limit of electron flux on the resistive anode (by monitoring the count rate on the position analyzer). Alignment of the secondary spectrometer of the XES endstation and calibration of the detectable energy range for the detector can also be performed with the elastic scattering light from the KCl sample. Since the scattering light has enough high intensity, it could be monitored by using the analog X-Y oscilloscope or by observing near “real-time” image recorded by the digital data acquisition system, in which the later gives better resolutions. In Figure 5.3 are digital pictures of spot of light diffracted from Si (111) wafer and the elastic scattering light from KCl, measured at photon energy of 2800 eV in 30 and 300 seconds, respectively. The position of the detector can be adjusted to define relative positions of the light spot with regards to the X-Y coordinate system of the 2-D image. The relationship between the photon energy and relative positions of the light spot on the image therefore can be established.

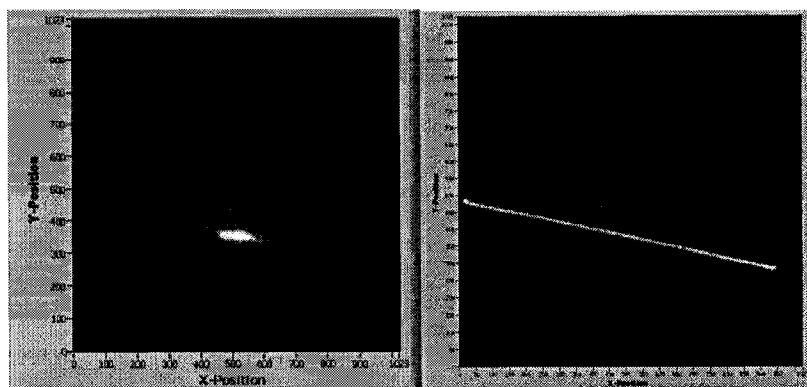


Figure 5.3: Image of the light spot from Si (111) wafer and elastic scattering light from KCl sample measured at 45° configuration of the spectrometer.

* Energy calibration and energy resolution:

The detectable energy range of the detector has been determined by using both elastic scattering light from the KCl sample and light diffracted from a Si (111) wafer mounted on the sample holder. The 45° configuration of the spectrometer is set and fixed. Photon energy is scanned in the range of 2785-2840 eV with a 5 eV-step. The images of the scattering light are captured by data acquisition system for both KCl sample and Si (111) wafer with the time of 300 sec and 60 sec, respectively. For KCl, the lines of the scattering light are observed only with photon energies in the range of 2790-2810 eV, while for Si(111), the light spots are observed in all measured energies. This can be explained by the fact that near and above the chlorine absorption edge (about 2824 eV for KCl), the KCl sample strongly absorbs the incident light and therefore less light scattered out from the sample. The absorption of light in a long period of time (>120 min) also leads to changing color of the sample, probably due to the “heating-up” process. Light diffracted from the Si (111) wafer is not affected by absorption process. The relative positions on the Y-axis of light spots on the images are given in Table 5.1, where for Si

the positions are measured at both center of the spot and at intersection with the Y-axis and for KCl the positions are the intersections of light with the Y-axis.

Table 5.1: Position on Y-axis of the spot lights elastically scattered from the KCl sample and diffracted from Si (111) wafer.

Energy	Si (Intersection)	Si (Center)	KCl (Intersection)
2840	935	800	
2835	880	740	
2830	820	695	
2825	770	640	
2820	705	585	
2815	670	530	
2810	600	470	700
2805	540	420	655
2800	480	370	575
2795	420	300	
2790	365	230	480
2785	305	180	

An estimation of 12 channels per electron-volt is obtained from Table 5.1. Thus for 1024 channels on Y-axis, the detectable range of energy is estimated about 85 eV. A detectable range of 55 eV has been observed experimentally as shown in Table 5.1. If we subtract a range of 150 channels from the top and bottom edge of the active surface of the detector to exclude the edge effects, an energy range of 60 eV (and thus the range of XES

spectrum) can be observed for this detector system with the photon energy in the vicinity of Cl K edge. The 2.6 channels spatial resolution of the detector corresponds to an estimated energy resolution of 0.22 eV

* Spectral resolution: The width of the line recorded from elastic scattering light of the KCl sample is estimated about 10 channels on the energy dispersion axis (Y-axis) as seen in Fig. 5.3, that give a spectral resolution of 0.83 eV

* Angular-dependence:

The angular dependence of elastic scattering light from the KCl sample has been measured at photon energy 2800 eV by rotating the spectrometer around B-axis of Figure 4.1 with a 10° -rotation step. Figure 5.4 shows graph of the total number of photons measured in 300 sec as function of rotation angles.

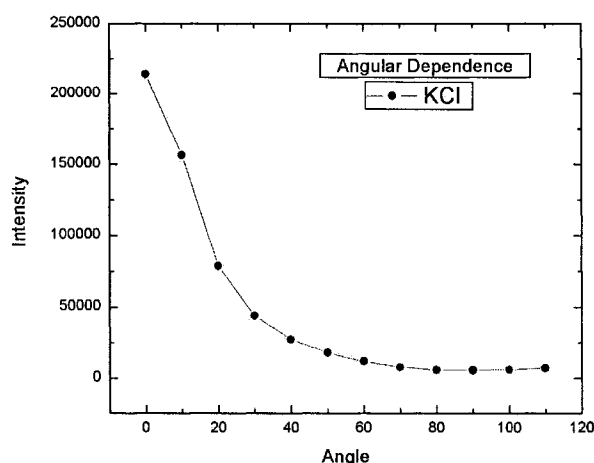


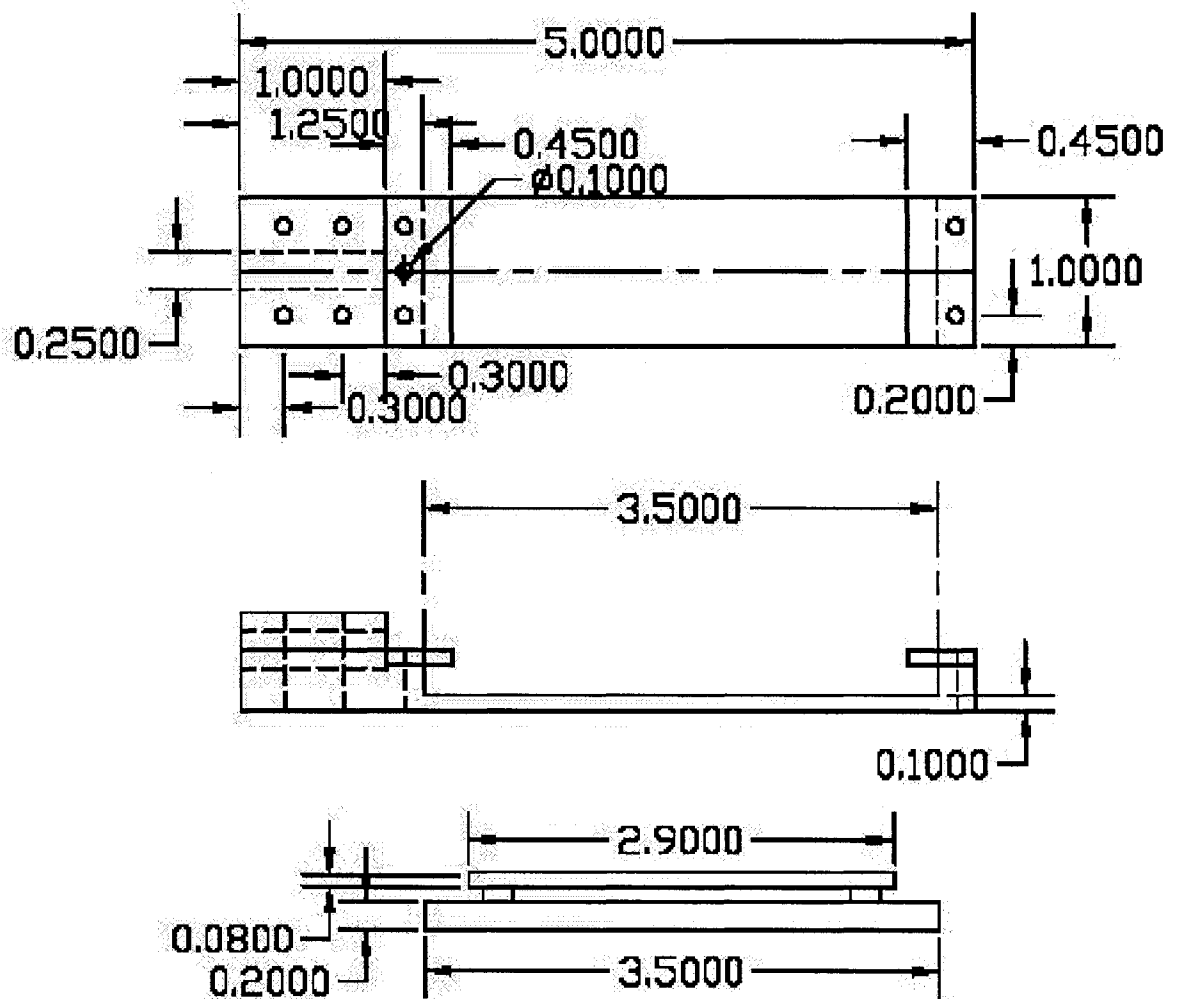
Figure 5.4: Angular dependence measurement using elastic scattering x-rays from KCl sample

If we assume that the incident light is linear polarized on the horizontal plane (plane of the storage ring), then I_0 , the total number of photons at 0° (parallel) represents for the intensity of light with contribution from linear, circular and unpolarized light components

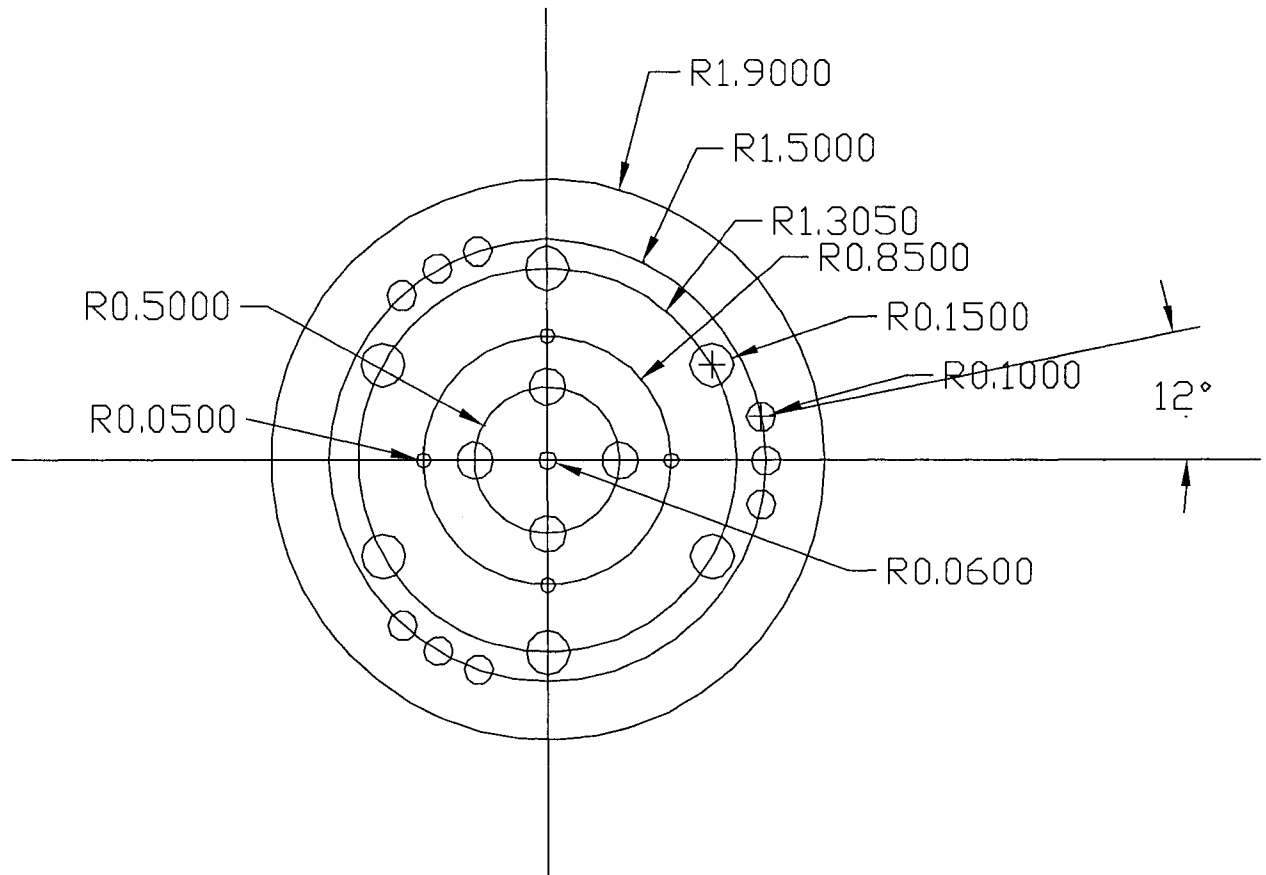
(I_{total}), and I_{90} , the total number of photons at 90° (perpendicular), represents for all non-linear polarized components of light (including unpolarized and circular). The polarization coefficient P of the incident beam then can be defined as: $P = \frac{I_0 - I_{90}}{I_0}$. From the angular-dependence measurement of the elastic scattering light from the KCl sample, an estimated polarization of 98% is obtained, below the expected polarization of 99.9% for the beamline in the energy range near Cl K edge. Misalignment of the spectrometer with respect to the beamline could affect the present polarization measurement. More detailed and accurate polarization measurements [56,57] would give better estimations of the polarization of the beamline. However, the present angular-dependence measurement demonstrates the principle of the technique and applicability of the x-ray emission spectrometer in polarization-sensitivity studies.

APPENDIX

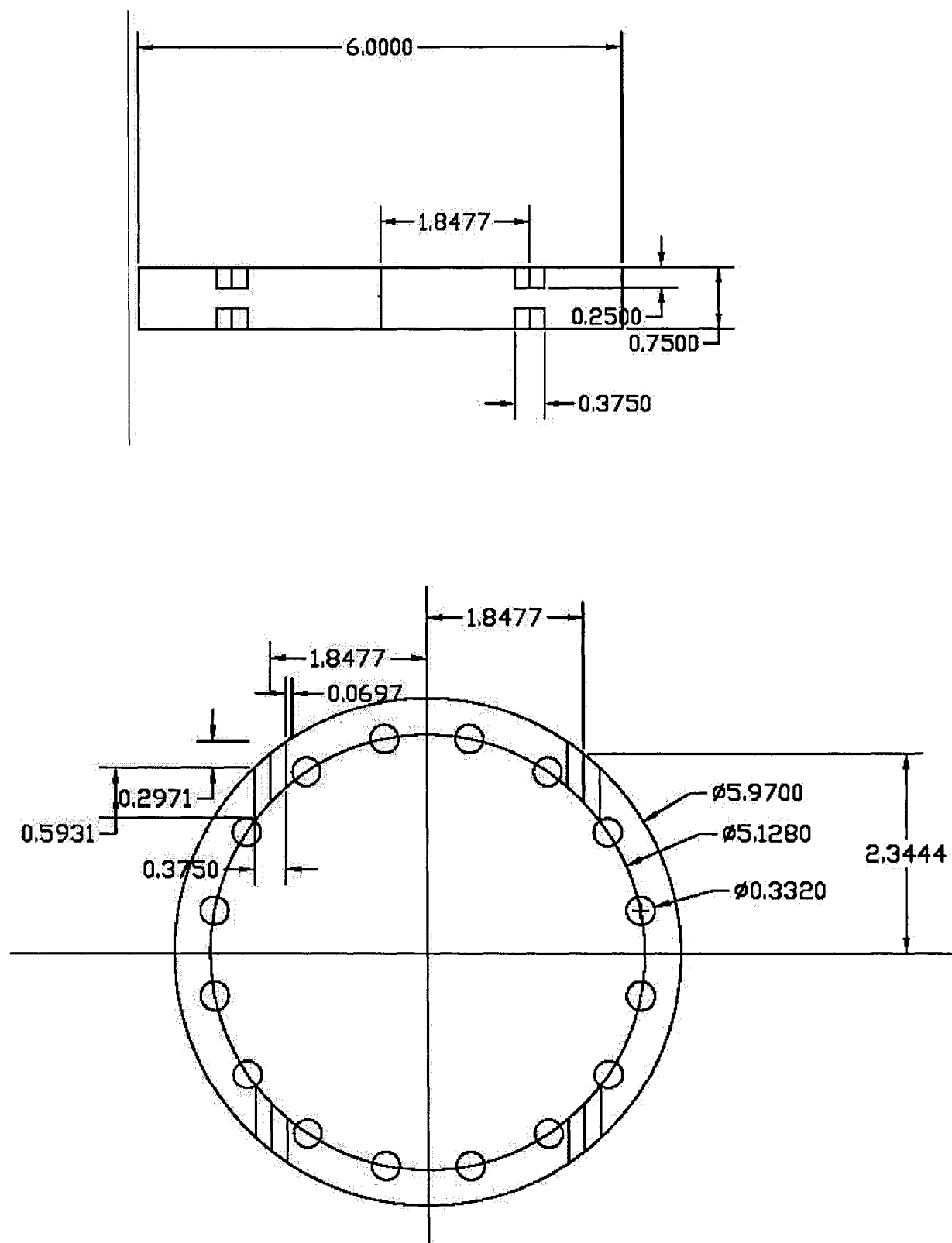
1. Design of the sample holder:



2. Design of the base-plate for detector mounting:

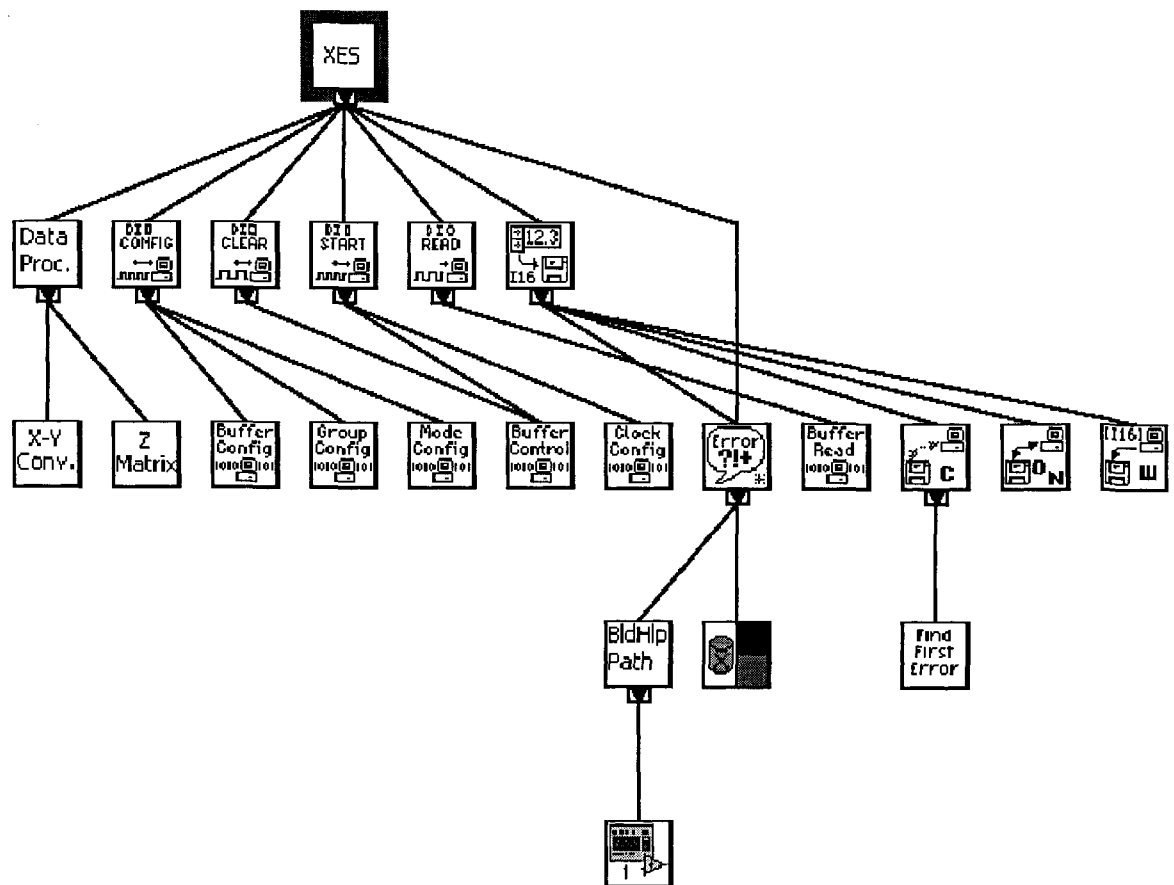


3. Design of the handles and vacuum flange for the detector

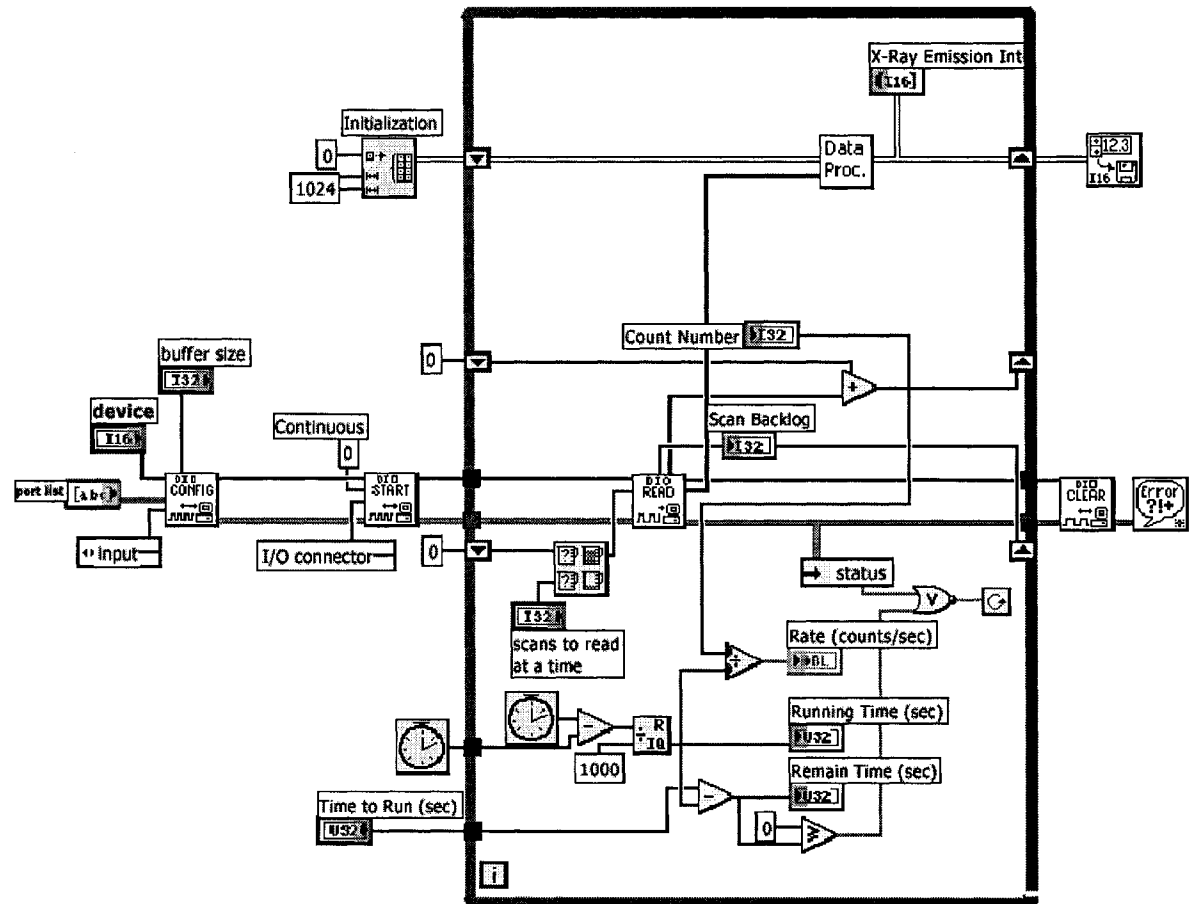


4. Data Acquisition Software:

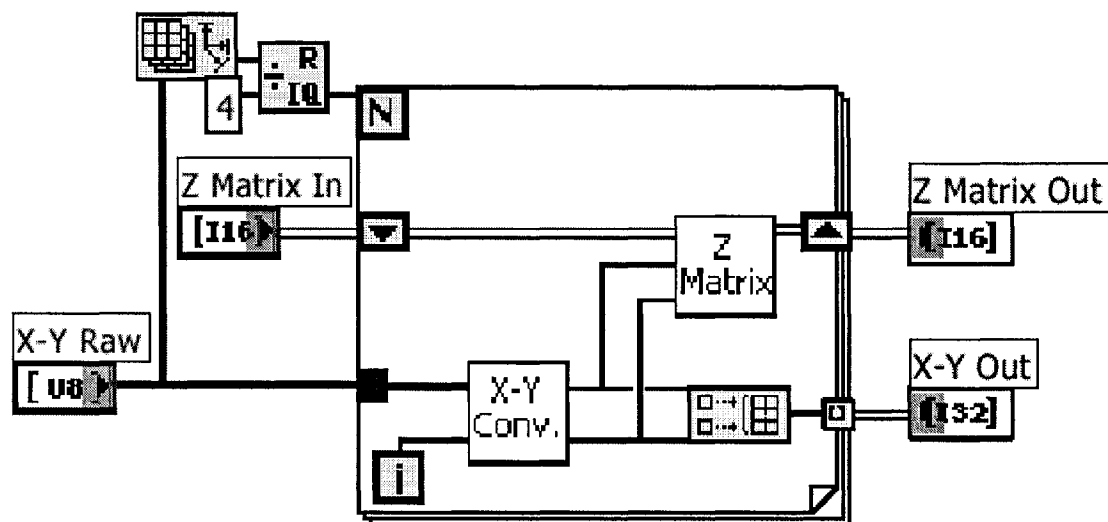
4.a. Hierarchy diagram:



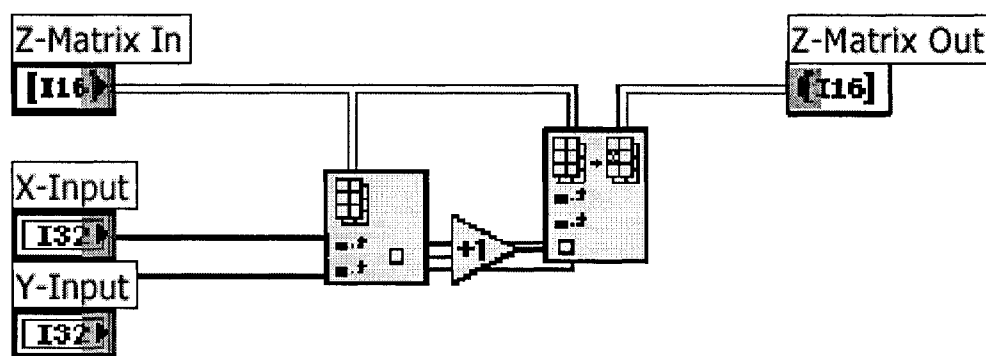
Reproduced with permission of the copyright owner. Further reproduction prohibited without permission.



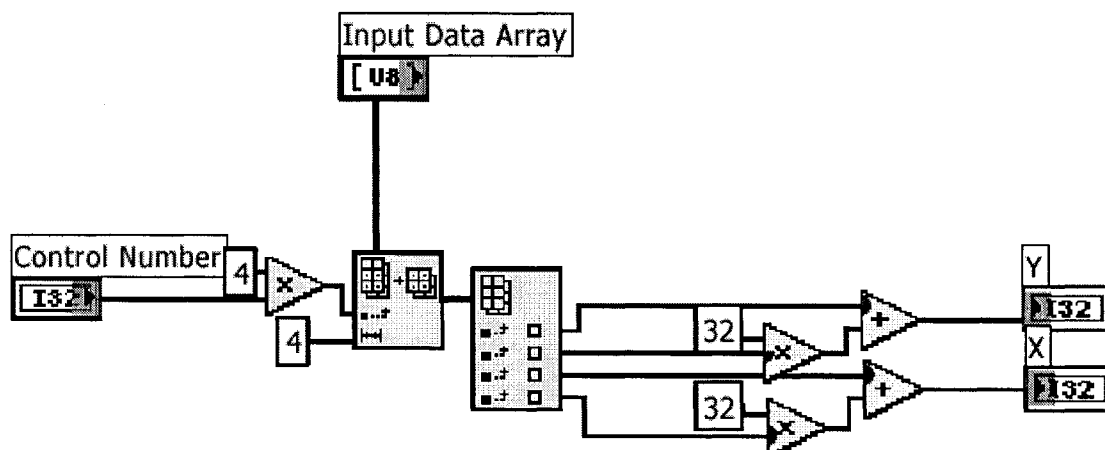
4.c. Data Processing:



4.d. Z-matrix:



4.e. X-Y Conversion:



BIBLIOGRAPHY

- [1] New directions in research with third-generation soft x-ray synchrotron radiation sources. Edited by: A.S. Schlachter and F. J. Wuilleumier. NATO ASI Series. Kluwer Academic Publisher, 1994
- [2] D.W. Lindle, P.L. Cowan, R.E. LaVilla, T. Jach, and R.D. Deslattes: Polarization of molecular x-ray fluorescence. *Phys. Rev. Lett.*, **60** (1988), pp. 1010-1013.
- [3] D.W. Lindle, B. Crasemann: Atomic, molecular, and optical physics with X-rays. *Nuclear Instruments and Methods in Physics Research Section B: Beam Interactions with Materials and Atoms*, **56-57** (1991), pp. 441-445.
- [4] J. Nordgren, G. Bray, S. Cramm, R. Nyholm: Soft x-ray emission spectroscopy using monochromatized synchrotron radiation. *Rev. Sci. Instrum.*, **60** (1989), pp. 1690-1696.
- [5] David Attwood: Soft x-rays and extreme ultraviolet radiation. Principles and Applications. Cambridge University press, 1999.
- [6] J. Nordgren, J. Guo: Instrumentation for soft x-ray emission spectroscopy. *J. Electron Spectr. Related Phenom.*, **110-111** (2000), pp. 1-13.
- [7] J.D. Mills, J.A. Sheehy, T.A. Ferrett, S.H. Southworth, R. Mayer, D.W. Lindle, and P.W. Langhoff: Nondipole resonant x-ray Raman spectroscopy: Polarized inelastic scattering at the *K* edge of Cl₂. *Phys. Rev. Lett.*, **79** (1997), pp. 383-386.
- [8] R.C.C Perera, P.L. Cowan, D.W. Lindle, R.E. LaVilla, T. Jach ,and R.D. Deslattes: Molecular-orbital studies via satellite-free x-ray fluorescence: Cl *K* absorption and *K*-valence-level emission spectra of chlorofluoromethanes. *Phys. Rev. A*, **43** (1991), pp. 3609-3618.
- [9] S.H. Southworth, D.W. Lindle, R. Mayer, and P.L. Cowan: Anisotropy of polarized x-ray emission from molecules. *Phys. Rev. Lett.*, **67** (1991), pp. 1098-1101.
- [10] D.W. Lindle, P.L. Cowan, T. Jach, R.E. LaVilla, and R.D. Deslattes: Polarized x-ray emission studies of methyl chloride and the chlorofluoromethanes. *Phys. Rev. A*, **43** (1991), pp. 2353-2366.

- [11] R. Mayer, D.W. Lindle, S.H. Southworth, and P.L. Cowan: Direct determination of molecular orbital symmetry of H₂S using polarized x-ray emission. *Phys. Rev. A*, **43** (1991), pp. 235-241.
- [12] K.E. Miyano, U. Arp, S.H. Southworth, T.E. Meehan, T.R. Walsh, and F.P. Larkins: Sulfur *K* β x-ray emission from carbonyl sulfide: Variations with polarization and excitation energy at the S *K* threshold. *Phys. Rev. A*, **57** (1998), pp. 2430-2435.
- [13] K. Gunnelin, P. Glans, P. Skytt, J.H. Guo, and J. Nordgren: Assigning x-ray absorption spectra by means of soft-x-ray emission spectroscopy. *Phys. Rev. A*, **57** (1998), pp. 864-872.
- [14] P. Glans, K. Gunnelin, P. Skytt, J. Guo, N. Wassdahl, and J. Nordgren: Resonant x-ray emission spectroscopy of molecular oxygen. *Phys. Rev. Lett.*, **76** (1996), pp. 2448-2451.
- [15] P. Skytt, P. Glans, D.C. Mancini, J.H. Guo, N. Wassdahl, and J. Nordgren: Angle-resolved soft x-ray fluorescence and absorption study of graphite. *Phys. Rev. B*, **50** (1994), pp. 10457-10461.
- [16] Y. Luo, H. Agren, and F. Gel'mukhanov: Polarization anisotropy in resonant x-ray emission from molecules. *Phys. Rev. A*, **53** (1996), pp. 1340-1348.
- [17] Y. Luo, H. Agren, and F. Gel'mukhanov: Symmetry assignments of occupied and unoccupied molecular orbitals through spectra of polarized resonance inelastic x-ray scattering. *J. Phys. B: At. Mol. Opt. Phys.*, **27** (1994), pp. 4169-4180.
- [18] S. H. Southworth, D. W. Lindle, R. Mayer and P. L. Cowan: Anisotropy of polarized X-ray emission from atoms and molecules. *Nuclear Instruments and Methods in Physics Research Section B: Beam Interactions with Materials and Atoms*, **56-57** (1991), pp. 304-308
- [19] "X-ray Atomic and Molecular Spectroscopy: Probing Fundamental Interactions between X-ray and Matter" – XAMS Group Research Project.
- [20] The instrument under development is based on an earlier design [48,49] with several improvements to enhance the combined resolution and throughput. More details about its overall design characteristics may be requested from Professor Dennis Lindle
- [21] Beamline 9.3.1–Technical specifications.
Web site: <http://www-als.lbl.gov/als/techspecs/bl9.3.1.html>.
- [22] P.W. Atkins – Molecular Quantum Mechanics. 2nd Edition. Oxford University Press, 1983

- [23] Akio Kotani: Theory of resonant x-ray emission spectra in strongly correlated electronic systems. *J. Electron Spectr. Related Pheom.* **110-111** (2000), pp. 197-212.
- [24] Faris Gel'mukhanov: Channel interference in resonance elastic x-ray scattering. *Phys. Rev. A*, **50** (1994), pp. 1129-1132.
- [25] Yanjun Ma: X-ray absorption, emission, and resonant inelastic scattering in solids. *Phys. Rev. B*, **49** (1994), pp. 5799-5805.
- [26] Frank M. F. de Groot : Multiplet effects in resonant x-ray emission. *AIP Conf. Proc.* **514**, 3 (2000)
- [27] P.W. Atkins – Physical Chemistry. 7th Edition. 2002
- [28] R.D. Deslattes, R.E. LaVilla, P.L. Cowan, and A. Henins: Threshold studies of a multivacancy process in the $K\beta$ region of Argon. *Phys. Rev. A*, **27** (1983), pp. 923-933.
- [29] U. Fano and J.H. Macek: Impact Excitation and polarization of emitted light. *Rev. Modern Phys.*, **45** (1973), pp. 553-573.
- [30] C. D. Caldwell and R.N. Zare: Alignment of Cd atoms by photoionization. *Phys. Rev. A*, **16** (1977), pp. 255-262.
- [31] H. Agren, F. Gel'mukhanov: Kramers-Heisenberg and Weisskopf-Wigner descriptions of resonant x-ray Raman scattering. *J. Electron Spectr. Related Pheom.* **110-111** (2000), pp. 153-178.
- [32] T. Privalov, F. Gel'mukhanov, and H. Agren: X-ray Raman scattering from molecules and solids in the framework of the Mahan-Nozieres-De Dominicis model. *Phys. Rev. B*, **64** (2001), pp. 165116-1, 16.
- [33] Faris Gel'mukhanov, Hans Agren: Resonant inelastic x-ray scattering with symmetry-selective excitation. *Phys. Rev. A*, **49** (1994), pp. 4378-4389.
- [34] K. Gunnelin, P. Glans, P. Skytt, J.H. Guo, and J. Nordgren: Assigning x-ray absorption spectra by means of soft-x-ray emission spectroscopy. *Phys. Rev. A*, **57** (1998), pp. 864-872.
- [35] A. Cesar, F. Gel'mukhanov, Y. Luo, H. Agren, P. Skytt, P. Glans, J. Guo, K. Gunnelin, and J. Nordgren: Resonant x-ray scattering beyond the Born-Oppenheimer approximation: Symmetry breaking in the oxygen resonant x-ray emission spectrum of carbon dioxide. *J. Chem. Phys.*, **106** (1997), pp. 3439-3456.

- [36] P. Skytt, P. Glans, J.H. Guo, K. Gunnelin, C. Sathe, J. Nordgren, F. Kh. Gel'mukhanov: Quenching of symmetry breaking in resonant inelastic x-ray scattering by detuned excitation. *Phys. Rev. Lett.*, **77** (1996), pp. 5035-5038.
- [37] M. Magnuson, S.M. Butorin, J.H. Guo, and J. Nordgren: Electronic structure investigation of CoO by means of soft x-ray scattering. *Phys. Rev. B*, **65** (2002), pp. 205106-1, 5.
- [38] Y. Luo, H. Agren, and F. Gel'mukhanov: Symmetry-selective resonants inelastic x-ray scattering of C₆₀. *Phys. Rev. B*, **52** (1995), pp. 14479-14496.
- [39] Akio Kotani and Shik Shin: Resonant inelastic scattering spectra for electrons in solids. *Rev. Modern Phys.*, **73** (2001), pp. 203-246.
- [40] E.D. Poliakoff, J.L. Dehmer, Dan Dill, A.C. Parr, K.H. Jackson and R.N. Zare: Polarization of fluorescence following molecular photoionization. *Phys. Rev. Lett.*, **46** (1981), pp. 907-910.
- [41] Ira N. Levine: Quantum Chemistry. Prentice Hall, 2000
- [42] Ira N. Levin: Molecular spectroscopy. John Willey & Sons, 1975
- [43] "Gaussian 03 User's Reference and IOps Reference"; "Exploring Chemistry with Electronic Structure Methods"; "Ab Initio Molecular Orbital Theory". Gaussian Inc.
- [44] WebMO-Computational chemistry on the web. Web site: <http://www.webmo.net/>
- [45] Hyperchem, ver.7.0. Product manual, HyperCube Inc.
- [46] C. Kittel: Solid State Physics. 7th Edition,
- [47] The STUTTGART TB-LMTO-ASA program. Web site: <http://www.mpi-stuttgart.mpg.de/andersen/LMTODOC/LMTODOC.html>
- [48] S. Brennan, P.L. Cowan, R.D. Deslattes, A. Henins, D.W. Lindle, and B.A. Karlin: Performance of a tuneable secondary x-ray spectrometer. *Rev. Sci. Instrum.*, **60** (1989), pp. 2243-2246.
- [49] A. Henins: Variable radius curved crystal mount. *Rev. Sci. Instrum.*, **58** (1987), pp. 1173-1176.
- [50] Quantar Technology 3300/2400 series. Product Manuals.
- [51] NI 653x: Product Manual. National Instrument Inc.,

- [52] SCB-68: Product Manual. National Instrument Inc.,
- [53] “LabVIEW Application Builder User Guide” and “LabVIEW-Product Manuals”. National Instrument Inc.,
- [54] L.G. Parratt and E.L.Jossem: X-ray spectroscopy of the solid state: Potassium chloride. *Phys. Rev. A*, **97** (1955), pp. 916-926.
- [55] K.E. Miyano, Y.Ma, S.H. Southworth, P.L. Cowan, and B.A. Karlin: Resonant Raman scattering in potassium and chlorine $K\beta$ x-ray emission from KCl. *Phys. Rev. B*, **54** (1996), pp.12022-12028.
- [56] J.A.R. Samson and A.F. Starace: Effect of elliptically polarized light on the angular distribution of photoelectrons. *J. Phys. B*, **8** (1975), pp. 1806-1809
- [57] V. Schmidt: Electron spectrometry of atoms using synchrotron radiation. Cambridge ; New York : Cambridge University Press, 1997.

VITA
Graduate College
University of Nevada, Las Vegas

Ich C. Tran

Local Address:

4247 Cottage Cir., Apt. 9
Las Vegas, NV 89119

Home Address:

121A Mai Hac De St.,
Hanoi, Vietnam

Degree:

Bachelor of Science: Engineer in Physics, 1984
Hanoi University of Technology, Hanoi, Vietnam

Thesis Title: X-ray Emission Spectroscopic Study of Solid Chloride Compounds Using
Synchrotron Radiation.

Thesis Examination Committee:

Chairperson, Dr. Dennis Lindle, Ph.D.
Committee Member, Dr. Oliver Hemmers, Ph.D.
Committee Member, Dr. Kathleen Robins, Ph.D.
Graduate Faculty Representative, Dr. James Selser, Ph.D.